Additive Manufacturing of Highly Alloyed Aluminum–Lithium

Lisa Matthäus,* Hagen Peter Kohl, Dongmei Liu, Stephanie Lippmann, and Stefan Nolte

Aluminum–lithium alloys offer significant potential for lightweight construction, exhibiting decreased density and improved specific stiffness as the lithium content increases. The specific stiffness of these alloys improves with lithium concentrations up to 14 at%, outperforming that of pure aluminum. However, traditional casting methods, constrained by low cooling rates, result in the precipitation of brittle AlLi phases at grain boundaries when the lithium content exceeds 9 at%, limiting further enhancements in stiffness. In this work, it presents laser-assisted additive manufacturing of binary Al–Li alloy powder with an increased lithium content of 14 at%. Unlike standard methods, this study utilizes an ultrashort pulse laser with a pulse duration of 250 fs at a wavelength of 1030 nm for the powder bed fusion process. With an average power of 150 W and a repetition rate of 32.5 MHz, it successfully demonstrates the production of highly dense Al-Li alloy specimens. Ex situ laser-induced breakdown spectroscopy is conducted to verify the high lithium content of the additively manufactured samples. Mechanical properties are assessed by measuring the elastic modulus and hardness. In addition, computer tomography, electron microscopy, and X-ray diffraction techniques are utilized for quantitative porosity analysis and to characterize microstructure and constituent phases.

1. Introduction

Energy and cost savings have a significant impact on industrial developments. Efficient energy use plays a central role because it not only reduces cost but also contributes to reducing environmental impact by decreasing resource consumption and emission. Therefore, weight reduction is a major driving force for developments in transportation, especially in the aerospace industry.

There are two major approaches to realize or even further improve the performance of light-weight parts for aircraft and spacecraft. One way is the use of additive manufacturing (AM), which allows the optimization of structure design with regard to the weight reduction. On the other hand, the material used can be modified or new materials with desired properties can be implemented.

For this reason, Al–Li alloys have received increasing attention for light-weight applications in the aerospace industry, recently.[1–3] The special feature of Al–Li alloys is not only the low density caused by the lightest metallic alloying element, lithium, but also the high specific stiffness of this material. The usage of such high stiff materials for aircraft components consequently enables further reduction in material and especially weight.[4]

The lithium concentration plays a crucial role for the properties and performance of the alloy. By adding lithium to aluminum, the alloy's strength, fracture toughness, and stiffness are improved.[2,5,6] The specific stiffness Φ of the Al–Li alloys, which depends on the ratio between the elastic modulus E and the density ρ $\left(\Phi \propto \frac{E}{\rho}\right)$, is enhanced for higher Lithium concentrations. Thus, for the binary Al-14at%Li alloy, a decrease in density by 5% is accompanied by a 30% increase in stiffness, compared to pure aluminum.[5,6]

A lithium content of 14 at% is the saturation concentration for the solution of Lithium in the α-Al-phase. However, in conventional Al–Li alloys, the lithium content is typically below 9 at%, because the production poses several challenges.[7–9] First, lithium is highly reactive and has a low boiling point, which requires precise control of the manufacturing conditions.[4] Second, the with increasing Li content increasing solidification interval causes segregations and makes it challenging to achieve a homogeneous distribution of lithium in the alloy. Segregation have a negative impact on mechanical properties.[9] For instance, the formation of the brittle intermetallic δ-AlLi phase can occur, resulting in a reduction in strength.[10]

Rapid solidification technologies have the potential to decrease the formation of segregations resulting in microstructures with

L. Matthäus, H. P. Kohl, D. Liu, S. Lippmann, S. Nolte
Friedrich Schiller University Jena
Institute of Applied Physics
Abbe Center of Photonics
Albert-Einstein-Str. 15, 07745 Jena, Germany
E-mail: lisa.matthaeus@uni-jena.de

S. Nolte
Fraunhofer Institute for Applied Optics and Precision Engineering IOF
Albert-Einstein-Str. 7, 07745 Jena, Germany

improved mechanical properties.[2,4,11] The cooling rates of such processes generally range from 10^3 to 10^6 K s^{-1}.[11] Given that laser-based powder bed fusion (PBF-LB) provides high cooling rates, up to 10^6 K s^{-1},[12–14] it represents a promising method for processing Al–Li alloys.

Although laser-based AM of traditional Aluminum alloys, such as AlSi, has been extensively studied, there are only a few studies on the PBF-LB process of Al–Li alloys.[15] Generally, existing publications present investigations on multicomponent alloys with lithium concentrations below 9 at%.[16–19] In 2020, we performed first investigations on laser powder bed fusion of binary Al–Li alloys with an ultrashort pulse laser (USP).[20] The work of Ullsperger et al. had shown that the use of USP lasers is a promising approach for the PBF-LB process of high-stiffness aluminum alloys.[21]

Ullsperger et al. observed an enhanced refinement of the microstructure accompanied by improved mechanical performance for hypereutectic Al–Si manufactured with an USP laser.[21] As a consequence, the application of USP lasers shows the potential to avoid pronounced precipitation of lithium during the laser fusion process of highly alloyed Al–Li. In addition, due to the small heat affected zone, ultrashort pulses are suitable for precise control of the melt pool temperature, which is a critical parameter to avoid excessive evaporation of lithium during PBF-LB.

This study presents the AM of binary Al–Li alloys with a high lithium concentration and demonstrates laser-induced breakdown spectroscopy as a method to analyze the lithium concentration of additively manufactured parts. Specifically, ultrashort laser pulses were employed for the laser powder bed fusion of the highly alloyed Al–Li powder with a lithium content of 14 at%. A systematic study was carried out to identify the PBF-LB process parameters for the production of highly dense parts. The characterization of the density involved computer tomography and hydrostatic weighting. Hardness tests and measurement of elastic modulus were performed. Electron microscopy and X-ray diffraction techniques are utilized to characterize microstructure and constituent phases of PBF-LB specimens.

2. Experimental Section

2.1. Laser Powder Bed Fusion (PBF-LB)

As ultrashort pulse lasers have not been implemented yet in commercial AM-systems an in-house developed PBF-LB machine is used for the AM of the Al–Li alloy. The fully automated setup is highly customizable due to its modular nature, consisting of a standalone process chamber, where different laser sources and scanner systems can be integrated. For the melting of the Al–Li powder we used an USP laser from Active Fiber Systems GmbH (Jena, Germany). The system delivers an average output power of up to $P_{av} = 150$ W at a central wavelength of $\lambda = 1030$ nm with a minimal pulse duration of $\tau = 250$ fs. Pulse duration as well as the pulse repetition rate f_{rep} are adjustable in the ranges given in **Table 1**. The laser light is guided by a SCANLAB intelliSCAN 20 galvanometer scanner to the build platform in the process chamber. An F-theta objective with a focal length of 163 mm focuses the laser beam on the powder surface, yielding a laser spot diameter of 20 µm $(1/e^2)$. The construction of

Table 1. Laser specifications.

P_{av} [W]	λ [nm]	τ [ps]	f_{rep} [MHz]
up to 150	1030	0.25 to 20	up to 32.5

the process chamber is similar to that of commercial PBF-LB systems, with two counteracting linear axes to supply powder from a reservoir and lower the build platform. A third axis applies the powder from the reservoir onto the build platform. The build volume has a diameter of 105 mm and a height of 100 mm. To prevent oxidation during the AM process the chamber is flooded with Argon.

2.1.1. Powder

As mentioned above, the production of Al–Li alloys with a high lithium content is challenging due to the segregation effects of Li. Therefore, the lithium content of commercial Al–Li alloys is limited to 9 at%, while the maximum solubility of lithium in the α-Al phase is 14 at%. For this reason, binary Al-14 at%Li alloy was produced in-house. A detailed description of the process has already been published in.[10] In a first step, ingots were fabricated by melting aluminum and lithium granules of 99.99% purity in a steel crucible lined with graphite foil under Argon atmosphere (O_2 level < 2 ppm, H_2O level < 0.1 ppm) at a temperature of 70 °C (heating rate of 20 °C min^{-1}). The second step was the powder production out of the ingots, which was performed by Nanoval GmbH (Berlin, Germany) by means of gas atomization. The morphology of the resulting powder is shown in the scanning electron microscope (SEM) image in **Figure 1**a. The spherical powder exhibits a mean particle size of $d_{50} = 13$ µm (see Figure 1b).

2.1.2. Parameter Study

To determine the process window for the fabrication of dense Al–Li parts, thin wall structures and bulk samples were fabricated with the PBF-LB setup, explained above, using the USP laser. As shown in previous investigations,[21–23] the operation in a high repetition rate regime supports a stable melting process. Thus, the laser repetition rate was set to the maximum value of 32.5 MHz. In relation to the work of Ullsperger et al.[21] the use of a short pulse duration promotes the refinement of microstructure, which results in an enhancement of the mechanical properties. For this reason, the pulse duration was fixed to 250 fs.

The PBF-LB process was performed under an Argon atmosphere with an oxygen level below 1000 ppm. All additive manufactured structures were fabricated on an aluminum platform with a 3 mm high support structure. The support structure had a grid-like shape with a hatch distance of 750 µm.

Thin wall structures were generated by a layer-wise implementation of single line scans to find the appropriate line energy for a stable melting process (see **Figure 2**a). The line width w_{line} of these melting tracks or rather thin walls served to identify the line overlap (LO) for area scans. The influence of line overlap on the density of bulk specimens was investigated by varying hatch distances d_{hatch}

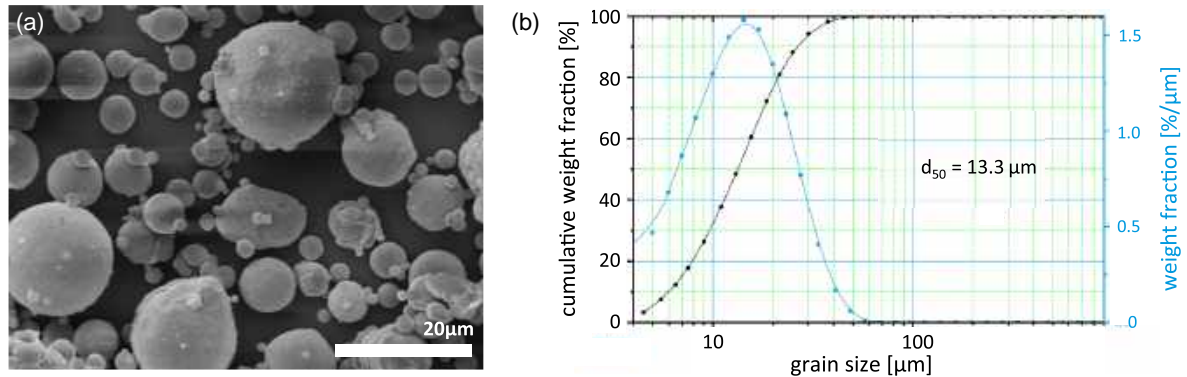$$LO = \left(1 - \frac{d_{hatch}}{w_{line}}\right) \qquad (1)$$

Figure 1. a) SEM image of Al-14 at%Li-powder. b) Particle size distribution showing a mean diameter of $d_{50} = 13\,\mu m$ and the 10th and 90th percentiles at $d_{10} = 5\,\mu m$ and $d_{90} = 28\,\mu m$, respectively.
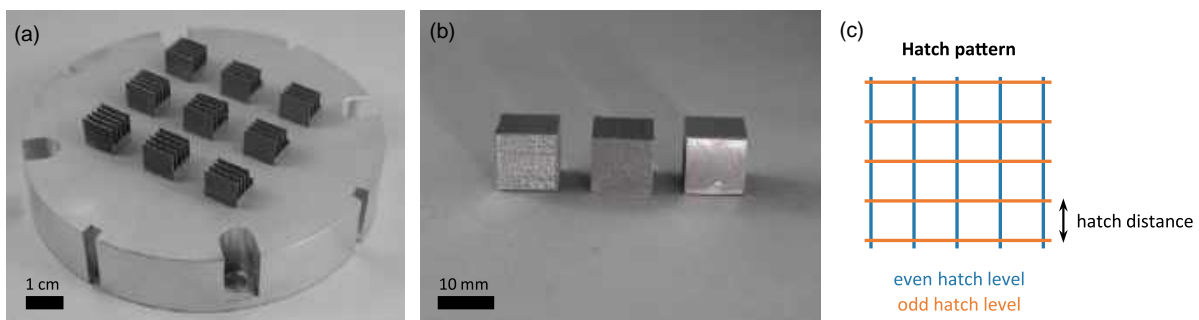

Figure 2. a) Image of samples from a line test, where laser power and scanning speed were varied for the fabrication of thin walls. The walls were built on top of a 3 mm high grid-like support structure on an aluminum platform. b) Image of three test samples showing the top surface, the surface parallel to the building direction and the bottom surface after removing the support structure by grinding (from left to right). c) Scheme of the hatch pattern applied for the fabrication of test specimens.

Therefore, small $3 \times 3 \times 3\,mm$ cubes were produced with a simple hatch pattern of parallel scanning lines (cf. Figure 2c). The line overlap was varied between 20% and 70%.

For mechanical characterization, larger cubes with an edge length of 10 mm were manufactured (cf. Figure 2b). Here, the hatch pattern was rotated by 90° from layer to layer. For all PBF-LB experiments, the layer thickness d_l was set to 20 μm.

2.2. Characterization

As this study investigates the feasibility of generating highly alloyed and dense Al–Li parts using the PBF-LB process, the characterization is mainly focused on the relative density or rather the filling factor and the lithium content of the additively fabricated parts. Both properties influence the mechanical properties and the microstructure, which are also analyzed in this work. In the following sections, the applied characterizations methods are explained.

2.2.1. Density Measurement

The determination of the density for the additive manufactured Al–Li alloy parts is not trivial, as a loss of lithium could occur during the PBF-LB process, and therefore the specific density of the material $\rho_{material}$ is unknown. One of the most prominent

quality criterions for AM is the relative density ρ_{rel} achieved. For samples with a known material composition, the absolute density ρ_{sample}, determined, e.g., by the Archimedes's principle, allows the calculation of the filling factor or rather the relative density ρ_{rel}

$$\rho_{rel} = \frac{\rho_{sample}}{\rho_{material}} \qquad (2)$$

However, this method does not work here, as the final Li content of our samples and, thus, the material density $\rho_{material}$ is unknown. Therefore, the absolute density of the samples ρ_{sample} was measured by hydrostatic weighing.[24] In addition, the relative density ρ_{rel} was determined by computer tomography (CT) analysis. This allows to determine the material density according to the relation given in Equation (2) and finally to extract the lithium content, described later (Section 2.2.2).

CT Analysis: The internal structure of the bulk specimens was investigated with a micro-CT system. This v—tome—x system from phoenix X-ray uses a cone beam arrangement with a nano-focus X-ray tube. 1440 different angles were recorded using an integration time of 2 s, an applied voltage of 95 kV, and a current of 150 μA. The voxel size obtained for the $1\,cm^3$ cubes was 9.35 μm.

For the relative density evaluation, the sectional images were analyzed and transformed into binary images, as presented in ref. [25]. The total relative density of one manufactured sample was calculated by the average filling factor of the sectional images.

Optical Inspection: Another way to determine the relative density is by extrapolation from the surface density, which can be classified by optical inspection of a polished cross section of the specimens. Assuming that the surface density ρ_{sur} is representative for all layers within the sample the relative density ρ_{rel} is simply given by

$$\rho_{rel} = \rho_{sur} \tag{3}$$

For the measurements, the samples were firstly embedded in epoxy resin and then grinded and polished. The same procedure was done for the additive manufactured thin wall structures to evaluate the line width w_{line} and calculate the line overlap (cf. Section 2.1.2). To evaluate the width of the thin-walled structures, an algorithm written in MATLAB was used. In a first step all microscopic images were converted to binary images. To measure only the width of the fused wall, all unconnected particles had to be removed. This was achieved using the *bwareaopen()* function in MATLAB, removing pixel-islands smaller than 50 000 px (corresponds to particles with a cross-sectional area of 19 000 μm^2). The width of the fused structure was then calculated for each row of pixels in the image. The width of the whole structure is then given by the median value of all rows and the standard deviation provides a measure for the width variability.

2.2.2. Determination of Lithium Content

For the binary Al–Li alloy, the lithium concentration of additively manufactured samples can easily be determined by the material density $\rho_{material}$. Assuming that lithium is completely dissolved in the α-Al phase, the lithium content c_{Li} can be extracted from the weight fraction calculation

$$\rho_{material} = (1 - c_{Li}) \cdot \rho_{Al} + c_{Li} \cdot \rho_{Li} \tag{4}$$

Here, ρ_{Al} and ρ_{Li} are the material densities of aluminum and lithium, respectively.

Another method to determine the lithium content is atomic emission spectroscopy. In this study, ex situ laser-induced breakdown spectroscopy (LIBS) was carried out to prove the high lithium content of the additively manufactured specimens. LIBS is an analytical technique for elemental composition analysis. The principle of LIBS involves focusing a laser with high pulse energy onto the surface of a sample, which creates a localized plasma.[26] The elemental composition of the sample can be quantitatively deduced by analyzing the plasma emission spectrum, because it contains characteristic lines that correspond to the recombination of the excited atom species present in the sample.[27] The intensity of such emission lines generated by the transition from an excited state k to lower state i is as follows[28]

$$I_\lambda^{ki} = F C_S A_{ki} \frac{g_k}{U_S(T)} \exp \frac{-E_k}{k_B T} \tag{5}$$

F is an experimental parameter, C_S is the concentration of the emitting species, A_{ki} is the Einstein coefficient for spontaneous emission, g_k and E_k are the statistical weight and energy of the upper level k, k_B is the Boltzmann constant, and $U_S(T)$ is the partition function at the temperature T. Equation (5) shows the linear dependency of the line intensity on the concentration. Therefore, the ratio of the intensities of the material specific lines are also correlating linearly with the material fractions. For the quantitative analysis of the elementary concentrations, a calibration measurement is needed.

In this study, ingots with a lithium concentration of 6, 9, and 14 at% were fabricated in the same manner as described in Section 2.1.1. The LIBS spectra of these ingots served for a calibration curve. **Table 2** gives an overview about the observed emission lines of aluminum and lithium.

For the determination of the lithium content of the additive manufactured samples, the ratios of the Li-lines at 610 and 671 nm and the Al-line at 396 nm were analyzed.

The LIBS experiments were performed under Argon. The samples were moved with a xyz-stage, allowing multiple measurement at different positions at the sample. All investigated samples were polished to ensure a comparable energy deposition during the plasma generation. The same USP laser system, which is integrated in the PBF-LB setup, was used for LIBS analysis. The repetition rate was set to 20 kHz. The pulse energy and pulse duration used were 640 µJ and 250 fs, respectively. For each measurement, the samples were illuminated for 300 µs.

As shown in **Figure 3**, the emission light is detected by a spectrometer (Ocean Optics HR4000). By inserting a mirror into the beam path (in front of the spectrometer), the surface of the samples could be inspected on a microscopic scale to consider the influence of potentially appearing material inhomogeneities or voids on the spectral signal.

2.2.3. Mechanical Testing

For characterizing the mechanical performance of the additively manufactured bulk samples, the elastic modulus and Vickers hardness were experimentally determined. Therefore samples with an edge length of 10 mm were analyzed. The elastic modulus in and perpendicular to the building direction of the specimens was determined using acoustic resonance spectroscopy. An ultrasonic flaw detector (Krautkrämer USM 36) was utilized to measure the velocities of ultrasonic waves c_L and c_T in the

Table 2. LIBS lines.

Element	λ [nm]	Transition	Reference
Al I	394.4	$3^2 P^0_{1/2} \rightarrow 4^2 S_{1/2}$	[31–33]
Al I	396.1	$3^2 P^0_{3/2} \rightarrow 4^2 S_{1/2}$	[31–33]
Li I	610.3	$2^2 P^0_{1/2} \rightarrow 3^2 D_{3/2}$	[31–33]
Li I	670.8	$2^2 S_{1/2} \rightarrow 2^2 P^0_{3/2}$	[31]

**ADVANCED
SCIENCE NEWS**
www.advancedsciencenews.com

**ADVANCED
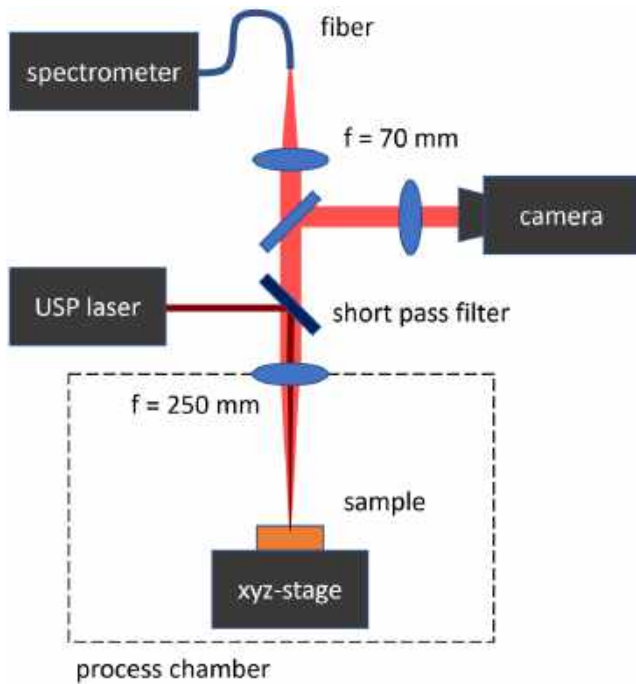ENGINEERING
MATERIALS**
www.aem-journal.com

Figure 3. Schematic of the experimental setup for LIBS characterization. For plasma generation, the test sample is illuminated with an USP laser within a process chamber. The emitted light is detected by a spectrometer through a low pass filter by an angle of incidence of 0°.

longitudinal and transversal direction, respectively. With the resulting Poission's ratio μ

$$\mu = \frac{c_L^2 - 2c_T^2}{2(c_L^2 - c_T^2)} \qquad (6)$$

and the measured density ρ (cf. Section 2.2.1) the elastic modulus was calculated according to[29]

$$E = \frac{\rho}{(1+\mu)} \cdot \sqrt{\frac{1-\mu}{2 \cdot (1-2\mu)}} \qquad (7)$$

Before the measurement of the elastic modulus, all surfaces of the samples were grounded metallographically using 1200 grit SiC paper.

Vickers hardness of the additive manufactured parts was also measured parallel and perpendicular to the building direction. Therefore, indentation hardness tests were performed using a diamond pyramid indenter with an apex angle of $\alpha = 136°$. A load of $F = 90.1\,N$ was applied to each polished surface. The Vickers hardness (HV) was then calculated from the average of the diagonals (d) and the applied test force (F)[30]

$$HV = \frac{0.102 \cdot F \cdot 2\sin(\alpha/2)}{d^2} \qquad (8)$$

For the orientations parallel and perpendicular to the building direction, three points for each surface were measured and the average value was used as the hardness of the surface.

2.2.4. Microstructure Characterization

The samples from PBF-LB process were prepared metallographically. Sample surfaces including the scanning surface and the surface along the building direction were ground with SiC abrasive paper successively up to 1200 grit and polished to a mirror finish with 9 µm, 3 µm, 1 µm, and 50 nm polycrystalline diamond suspensions. Following mechanical polishing, chemical etching was performed as described in the following. The sample was first etched using solution A (1 g NaOH + 100 mL H$_2$O) for 5 s and then washed in solution B (5 ml HNO$_3$ + 100 ml H$_2$O), followed by etching in the solution A for 1 min. First, the microstructure was analyzed by optical microscopy (OM). For microstructure analysis using secondary electron microscopy (SEM), a thin layer of gold was deposited on the surface of the sample by sputter coating to improve the electrical conductivity of the embedded samples and the reflectivity of the surface of the samples. For characterizing the constituent phases in the samples prepared by the PBF-LB process, X-ray diffraction (XRD) scans between 20° and 80° were performed.

3. Results

A detailed parameter study was carried out to optimize the PBF-LB process in relation to the generation of dense Al–Li alloy parts. As already mentioned, the repetition rate and pulse duration of the USP laser system were kept constant at 32 MHz and 250 fs. The layer thickness was always 20 µm. In a first step, single track walls were produced with different laser powers and scanning speeds (up to 130 W, 100−1800 mm s^{-1}). The processing with a laser spot diameter of 30 µm ($1/e^2$) resulted in stable melting lines with a gap in the center for almost all parameter sets (cf. **Figure 4**a). The gap was caused by laser ablation, indicating that the peak intensity was too high. Using a defocused beam with a $1/e^2$ spot diameter of 100 µm on the powder surface, the central gap was avoided, as the larger spot reduces the intensity by a factor of about 11.

Figure 4b gives an overview about the resulting melting quality of the single-track walls for different average powers and scan velocities. Below 56 W, average power stable walls could only be fabricated using a slow scanning speed below 500 mm s^{-1}. As illustrated in Figure 4b, there is a huge parameter range for medium laser powers (30−100 W), where the melting lines exhibit interruptions (*regime I*), like shown in Figure 4c. For laser power above 50 W and scan velocities below 500 mm s^{-1}, (*regime III*) voids within the melting track, and a significant sintering zone surrounding the wall occurred, as shown, for example, in Figure 4e. In a small process window with the maximum available laser power of 130 W and scan velocities between 500 and 1000 mm s^{-1} homogeneous melting could be achieved (*regime II*).

To identify the appropriate line overlap (cf. Equation (1)) for the fabrication of dense bulk samples, the wall thickness of the single tracks was investigated. The thickness was evaluated from binary images of the cross section by an algorithm that neglects the attached particles and cavities (cf. 2.2.1). A representative example is given in **Figure 5**b. The red line marks the determined edges of the wall. The wall thickness was calculated by the mean
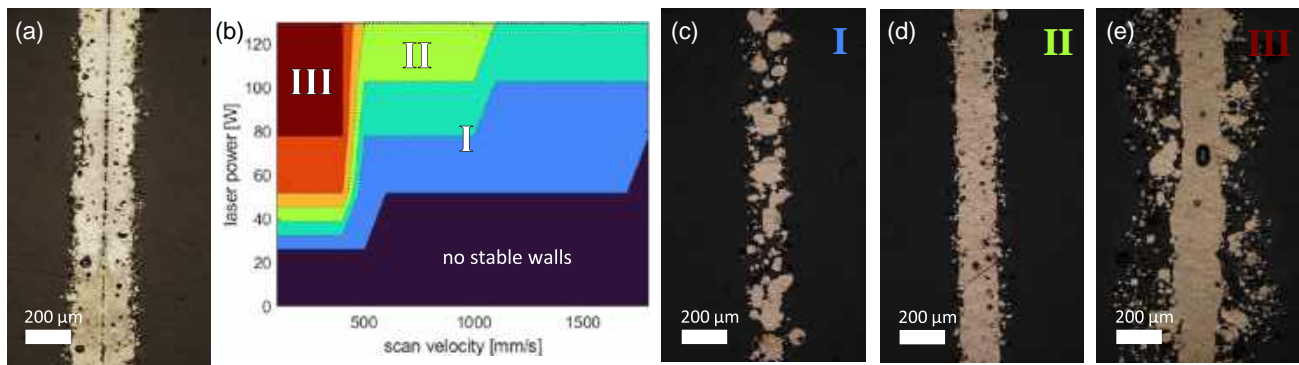
Figure 4. a) Microscope image of the polished cross section of a wall, fabricated with a small focal spot of 30 μm at $P_{av} = 115$ W and $v_{scan} = 500$ mm s^{-1}. b) Scheme of the resulting melting quality for single track walls for varied laser powers and scan velocities. Three different regimes can be distinguished. c–e) Optical microscope images of walls, which are representative for the regimes I, II, and III, fabricated with a spot diameter of 100 μm at $P_{av} = 26$ W and $v_{scan} = 1200$ mm s^{-1}, $P_{av} = 130$ W and $v_{scan} = 700$ mm s^{-1}, $P_{av} = 130$ W, and $v_{scan} = 100$ mm s^{-1}, respectively.
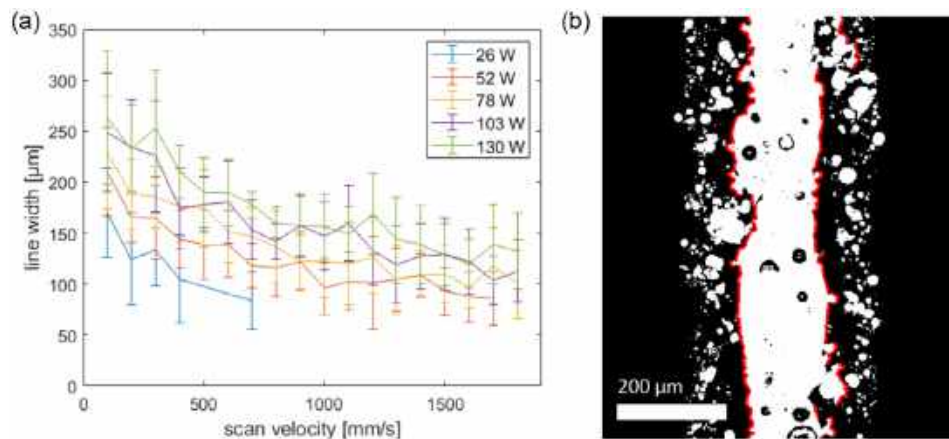

Figure 5. a) Diagram showing the thickness of single track walls as a function of the scanning velocity for different laser powers. b) Binary microscope image of the cross section of a wall fabricated at $P_{av} = 130$ W and $v_{scan} = 100$ mm s^{-1}. The red line marks the edges and is determined using the algorithm described in Section 2.2.1.

value of the varying wall width. The diagram in Figure 5a shows the wall thickness as a function of the scanning velocity for five different parameter sets of average laser powers. As expected, the wall thickness decreases for increasing scan velocity and decreasing laser power, i.e., the thickness increased with rising line energy $\left(\frac{P_{av}}{v_{scan}}\right)$. Thicknesses between 100 and 350 μm could be achieved in the parameter range studied.

To verify that the resulting parameters for the line tests can also be transferred to the volumetric specimen fabrication process, bulk sample tests were performed within the parameter field of laser power and scan velocities already introduced for varying line overlap (cf. **Figure 6**b). These tests revealed, as for the line tests, the same range of scanning velocities from 500 to 1000 mm s^{-1} that yields the best results in terms of the filling factor ρ_{rel}. Furthermore, the maximum laser power of $P_{av} = 130$ W allows for the bulk samples with the highest filling factor. Figures 6c–f shows images of polished bulk sample surfaces for different applied laser powers. Scan velocity and line overlap were kept constant at $v_{scan} = 500$ mm s^{-1} and LO = 70%, respectively. The scheme in Figure 6a shows that the observation plane is parallel to the building direction and

perpendicular to the orientation of the scanning lines, respectively. At maximum laser power the filling factor of >99% was reached (cf. Figures 6f).

The influence of line overlap on the density of the bulk parts is illustrated in **Figure 7**. Here, the overlap was varied between 10% and 70%. For small overlaps, no sufficient connection could be observed between two adjacent melting tracks, resulting in a lack of fusion parallel to the building direction. The distance between these elongated lacks of fusion porosities is equivalent to the hatch distance. As an example, Figure 7c reveals a hatch distance around 250 μm. To generate high densities, a line overlap above 60% is necessary. For 70% overlap the filling factor was 99.5% ± 0.1%. Higher line overlaps were not investigated intensively, due to following reasons. On the one hand side, a higher overlap means smaller hatch distances, for instance, an overlap above 70% would need a hatch distance around or rather below 50 μm. The resulting increase in processing time is incommensurate with the potential improvement of the relative density. Furthermore, because of the high energy input per area at lower hatch distances, balling effects and a straightening of the solidified melting tracks
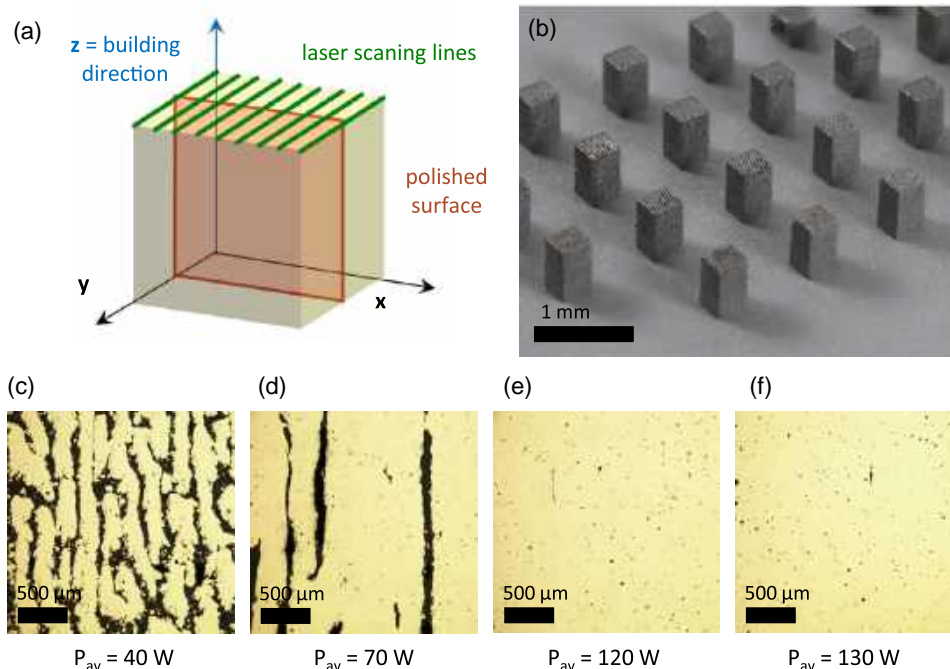
Figure 6. a) Scheme of a bulk sample indicating the relative orientation of building and hatch direction to the cross section, which was investigated concerning the surface density. b) Photograph of bulk samples from a parameter test as build on the aluminum platform. c–f) Microscope images of the cross section of bulk samples fabricated with different laser powers at constant scanning velocity and line overlap ($v_{scan} = 500\,mm\,s^{-1}$, LO = 60 %).
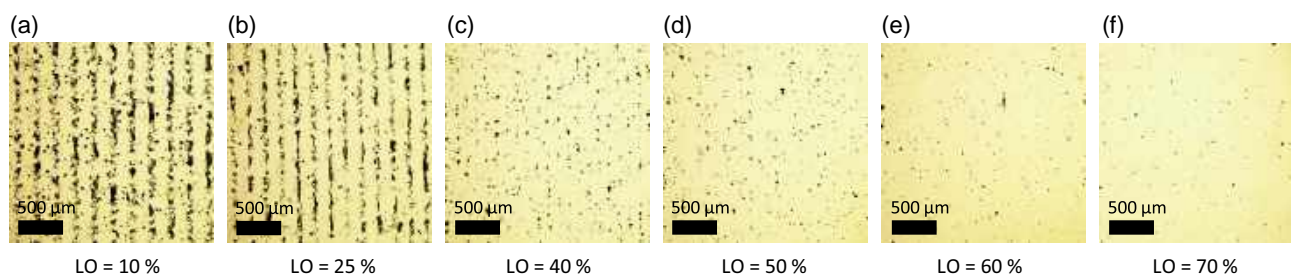

Figure 7. a–f) Microscope images of the polish cross section of different bulk samples fabricated with varying line overlap. Laser power and scanning velocity were kept constant ($P_{av} = 130\,W$, $v_{scan} = 500\,mm\,s^{-1}$).

became prominent within these ranges and prevented the fabrication of bigger parts.

3.1. Density Characterization

Within this identified processing window, test samples were manufactured that allowed for the versatile characterization of the density, as described in Chapter 2.2.1. In contrast to the previous bulk tests, the hatch pattern was rotated by 90° from layer to layer (cf. Chapter 2.1.2).

The sectional images of the CT data revealed that the surface density of the test samples was comparable to that previously measured by microscope inspection (cf. Figure 7f). In **Figure 8**, the results of the CT analysis are illustrated for a test sample, fabricated with $P_{av} = 130\,W$, $v_{scan} = 1000\,mm\,s^{-1}$, and LO = 70%. A typical sectional image oriented perpendicular to the building direction is shown in Figure 8a. The enlarged image

and its binary counterpart (Figure 8b,c) revealed pores with a diameter around a few tens of micrometers. Nevertheless, the calculated filling factor is still 99.6% ± 0.6%.

In **Table 3**, the results of the density characterization from the CT analysis and the hydrostatic weighting are summarized for three different test samples. Furthermore, the resulting material density of the Al–Li alloy is given. All relative densities were above 99%. Sample C exhibited the highest relative density of 99.7% and also the highest absolute density with $2.44 \pm 0.04\,g\,cm^{-3}$. The resulting material densities were above the theoretical value for Al-14at%Li at $2.4\,g\,cm^{-3}$, indicating a loss of Lithium during the PBF-LB process.

3.2. Lithium Concentration

Using EDS (X-ray energy dispersive spectrometry), which is a standard method for quantification the content of elements with
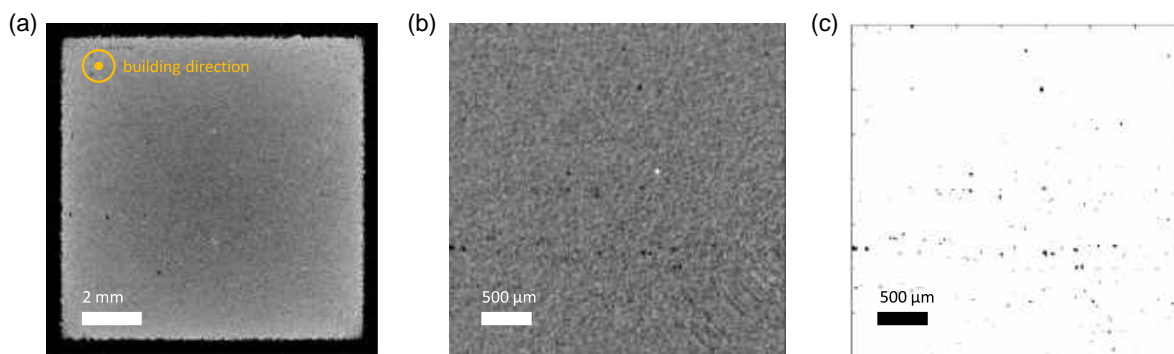
**ADVANCED
SCIENCE NEWS**

www.advancedsciencenews.com

**ADVANCED
ENGINEERING
MATERIALS**

www.aem-journal.com

Figure 8. a) Image of a test sample fabricated for CT analysis ($P_{av} = 130\,W$, $\nu_{scan} = 1000\,mm\,s^{-1}$, LO = 70%). b) Enlarged view of image shown in (a) and its binarized counterpart c). The material is colored white and pores are marked by black.

Table 3. Density characterization of test samples. The relative density ρ_{rel} results from the CT analysis. The absolute density ρ_{sample} was determined by hydrostatic weighting. $\rho_{material}$ and $c_\rho[Li]$ are the resulting material density and lithium concentration.

Sample	ν_{scan} [mm s^{-1}]	ρ_{rel} [%]	ρ_{sample} [g cm^{-3}]	$\rho_{material} = \rho_{sample} \cdot \rho_{rel}^{-1}$ [g cm^{-3}]	$c_\rho[Li]$ [at%]
A	500	99.5 ± 0.3	2.417 ± 0.040	2.429 ± 0.048	12.5 ± 2.2
B	700	99.4 ± 0.5	2.433 ± 0.040	2.449 ± 0.053	11.6 ± 2.5
C	1000	99.6 ± 0.6	2.440 ± 0.040	2.449 ± 0.054	11.6 ± 2.5

atomic number bigger than 5, is not straightforward for the quantification of the Li content. In the present work, an ex situ laser induced breakdown spectroscopy (LIBS) is employed to characterize the Li content of the additive manufactured test specimens. Here, the LIBS signal generated by a laser exposure for 300 μs with a pulse energy around 640 μJ at a repetition rate of 20 kHz was evaluated. The resulting spectra of the Al–Li alloy sample exhibited three prominent lines: The doublet Al I lines at 394 nm and 396 nm and two Li I lines at 610 and 671 nm, respectively. In **Figure 9**, the normalized spectra of three Al–Li ingots with known lithium concentration and one additively manufactured sample are shown. To visualize the dependence

of the lithium content on the amplitude of the material-specific lines, the spectra were normalized to the Al I line at 396 nm. The LIBS analysis of the ingot revealed that the peak intensity of both Li I lines increased compared to the Al I line with increasing lithium concentration. The ingot results served as a calibration measurement. Based on the spectral intensities shown in Figure 9, it is obvious that the lithium concentration of the additively manufactured specimen is slightly reduced and in-between 9 and 14 at%.

From a statistical analysis of the LIBS signal, the lithium concentration of the PBF-LB samples could be interpolated. Therefore, the LIBS spectrum at 20 different positions of one
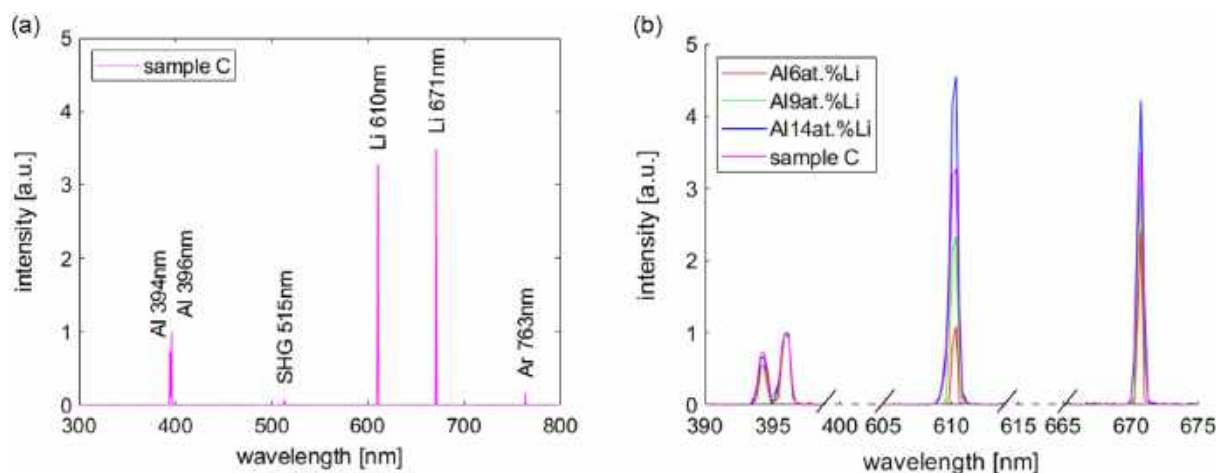

Figure 9. a) LIBS spectra of one PBF-LB sample fabricated at $P_{av} = 130\,W$ with $\nu_{scan} = 1000\,mm\,s^{-1}$ and LO = 70%. b) LIBS spectra of Al–Li ingots with a known lithium concentration and one PBF–LB sample normalized to the peak intensity of the Al I line at 396 nm.
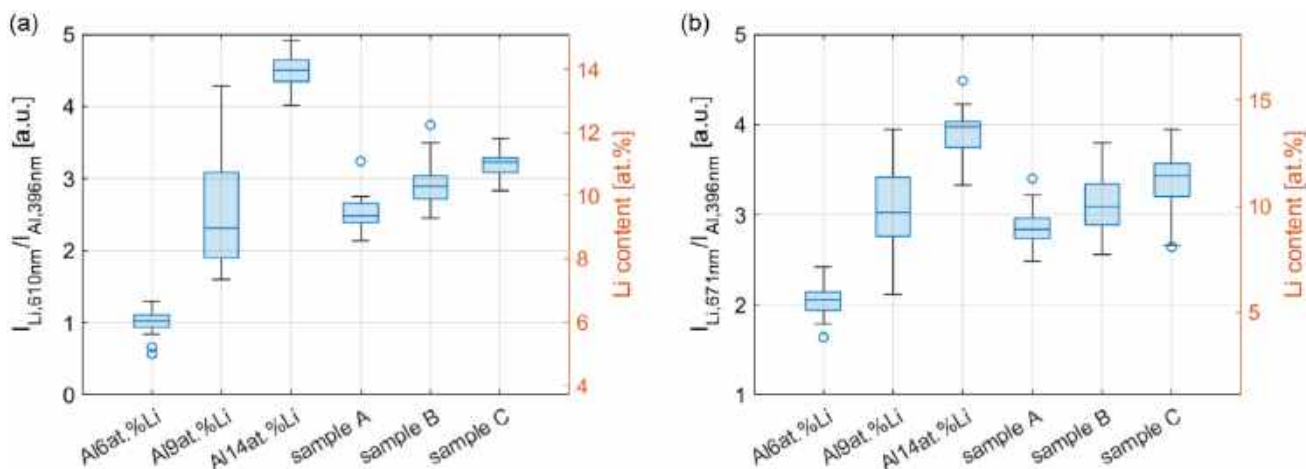
ADVANCED
SCIENCE NEWS
www.advancedsciencenews.com

ADVANCED
ENGINEERING
MATERIALS
www.aem-journal.com

Figure 10. Boxplots representing the evaluation of the peak intensity of the Li I lines at a) 610 nm and b) 671 nm in relation to the Al I line at 396 nm. For both cases, the interpolated Lithium concentration of the additively manufactured samples are in the range of 9–11.5 at%.

sample was measured. **Figure 10**a,b shows the quotient of the peak intensities of the Li I lines to the Al I line at 396 nm. As expected from Equation (5), the ingots show an increase of the relative spectral intensity with increasing lithium content. Furthermore, both lithium lines (610 and 671 nm) showed the same evolution for all given ingots and samples. According to the linear relation between the quotient of the peak intensities and the lithium concentration (Section 2.2.2), the lithium content of the additive manufactured parts can be derived from the median values. For sample C, processed at $P_{av} = 130\,W$ with $v_{scan} = 1000\,mm\,s^{-1}$ and LO = 70%, the highest lithium concentration of 11.2 ± 0.4 at% could be found. The calculation of this value included the evaluation of both lithium lines. Sample A and B revealed lithium concentrations of 9.1 ± 0.6 at% and 10.1 ± 0.7 at%, respectively. The only different processing parameter for the different specimens was the scanning velocity (cf. Table 3). A decreasing scanning velocity results in a higher lithium loss, which can be explained by a higher energy input and therefore higher temperatures during the melting process promoting lithium evaporation.

3.3. Mechanical Testing

To analyze the dependence of the Lithium content on the mechanical properties, the Vickers hardness and elastic modulus were measured. The results for the three samples A, B, and C are shown in **Table 4**. Furthermore, the values for a pure aluminum sample and two Al–Li ingots measured with the same setup are given (cf. Section 2.2.3). For samples A, B and C, no significant differences of the E-modulus and Vickers hardness in the two orientations parallel and perpendicular to the building direction could be found. This validates the isotropic structure of the specimens, which have already been revealed by the CT investigations. For the elastic modulus, as well as the Vickers hardness, the values of the additively manufactured samples were in between the two analyzed Al-Li ingots with 6 and 14 at% lithium concentration.

In **Figure 11**, images of the imprints are shown after hardness tests. In comparison with the as-cast samples, the edges in the

Table 4. E-modulus of test samples measured parallel and perpendicular to the building direction. The E-modulus for an aluminum sample and two Al-Li ingots with known lithium concentrations are given.

Sample	$E_{\parallel}$ [GPa]	$E_{\perp}$ [GPa]	$HV_{\parallel}$	$HV_{\perp}$
A	73.6	74.0	71.3	71.4
B	73.1	74.3	76.0	71.2
C	73.1	77.3	77.7	79.2
Sample	E [GPa]	–	HV	–
pure Al	68.0	–	15.0	–
Al-6 at%Li	72.5	–	25.7	–
Al-14 at%Li	81.1	–	104.3	–

PBF-LB samples are clearly deformed instead of flat and straight. This observation could be attributed to high stresses in the lattice caused by the rapid cooling rates in AM.

3.4. Microstructure

The microstructure of the three PBF-LB cubes is shown in **Figure 12**, which exhibits a layered structure composed of consecutive melting pools. Perpendicular to the building direction (Z), i.e., in the XY sectional view, elongated melting pools formed during the PBF-LB process. In the XZ view along the building direction Z, the layered structure with semicircular melting pools can be clearly seen. With increasing scanning speed, a higher density of melting tracks is observed, which is consistent with the reduced melting pool size at high scanning speed, as demonstrated by the single-wall line tests (c.f Figure 5). Melting pool tracks with a larger depth are randomly observed in the XZ view. This is accompanied by spherical pores (marked by the arrows), which may result from the keyhole effect and are supposed to be gas-trapped pores forming during solidification. Compared to sample A with a scanning speed of $500\,mm\,s^{-1}$, fewer pores were found in sample C with

ADVANCED
SCIENCE NEWS
www.advancedsciencenews.com

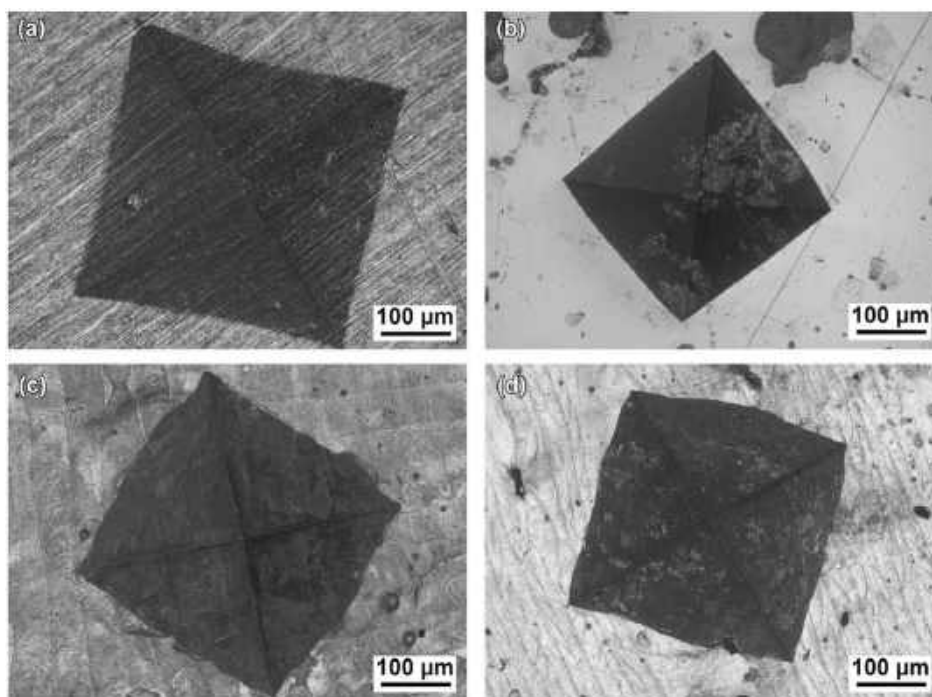ADVANCED
ENGINEERING
MATERIALS
www.aem-journal.com

Figure 11. OM images of the imprint after hardness test; a) Al-6at%Li ingot; b) Al-14at%Li ingot; c) Al-14at%Li, PBF-LB sample A; and d) Al-14at%Li PBF-LB sample C.
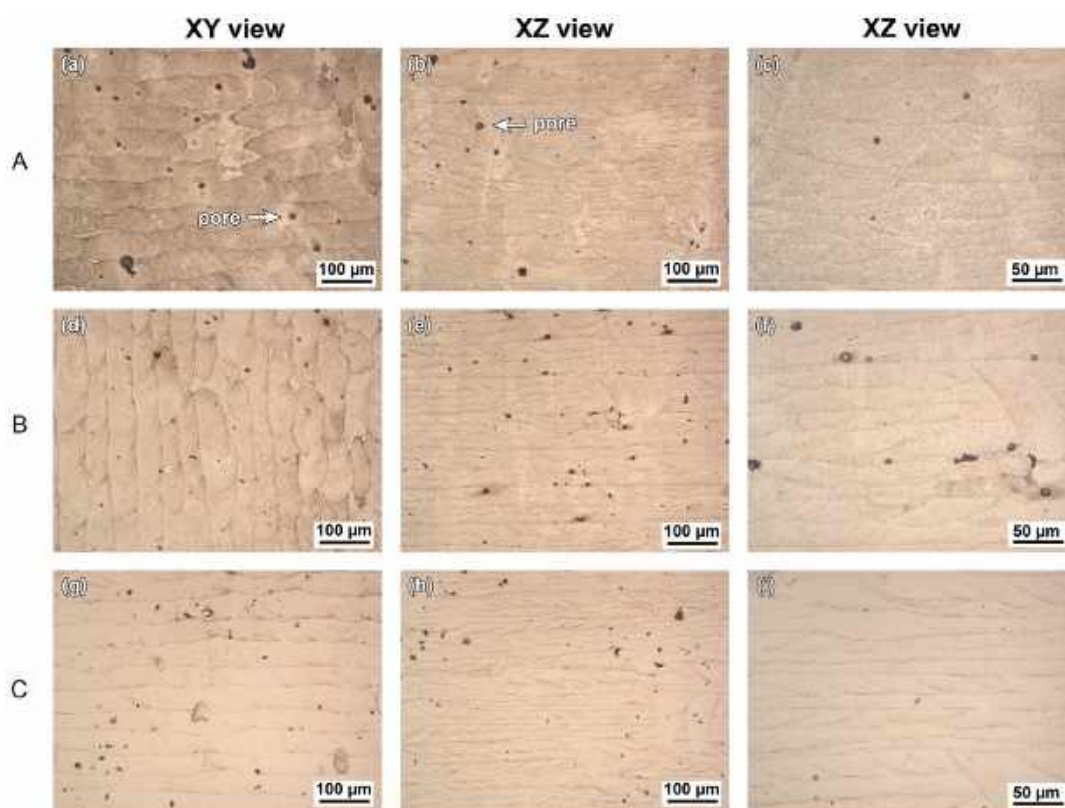

Figure 12. Optical microstructure of PBF-LB cubes fabricated at laser power $P_{av} = 130$ W at scanning speeds vs of 500 mm s^{-1} (sample A), 700 mm s^{-1} (sample B), and 1000 mm s^{-1} (sample C), illustrating the layered structure of the melting pools and the defects.

ADVANCED
SCIENCE NEWS

www.advancedsciencenews.com

ADVANCED
ENGINEERING
MATERIALS

www.aem-journal.com

a scanning speed 1000 mm s^{-1}. The reason is the resulting reduced line energy. Nevertheless, all these three samples exhibit a relative density higher than 99%.

The micrographs of cube C in **Figure 13**a,b show the microstructure after etching using optical microscopy at a magnification higher than that of Figure 12. Each melting pool (MP) track can be clearly seen, indicating an overlap of the MPs above 50% and the layered structure of the layer thickness 20 μm. It is worth noting that the MP boundary is much more prone to etching. This leads to the formation of very fine pores as a result of etching and makes microstructure analysis using a traditional metallographical method not feasible. This indicates either segregation (and the formation of intermetallic phases) or a high density of defects at the MP boundaries. As an alternative method, Ga ion beam milling was applied to polished samples to reveal the microstructure. An enrichment of Ga was found at MP boundaries, as shown in Figure 13c, probably resulting from the reaction of Gallium with Lithium forming intermetallic phase during preparation. This in turn indicates the segregation of Lithium at the MP boundaries. However, no coarse secondary phase was detected at the MP boundaries, ruling out the formation of δ-AlLi phase during PBF-LB processing. Inside the MP, there is nearly no big difference in brightness, indicating an even distribution of lithium, i.e., there is no obvious microscale lithium segregation. However, as shown in Figure 13d, ultrafine nanoscale black regions have been observed. These are probably the Al$_3$Li precipitates as discussed in the following.

The XRD results of the powder particles and the sample from PBF-LB process are shown in **Figure 14**. Both, powder particles and the sample from PBF-LB process, are mainly composed of
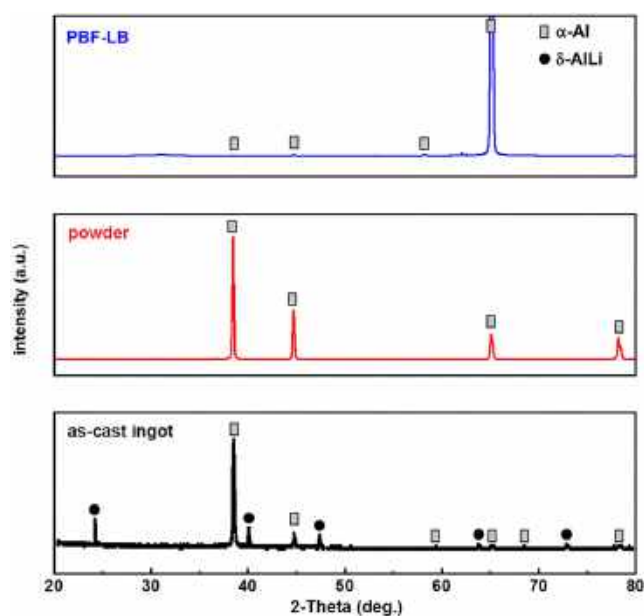

Figure 14. X-Ray diffractogram of the PBF-LB sample C, the powder and the as-cast ingot.

the α-Al phase. The δ-AlLi phase as observed in the as-cast ingot was not detected.[10] Nevertheless, the PBF-LB sample exhibits a very sharp peak at $2\theta = 65.1°$ corresponding to the (110) plane, indicating the presence of a well-ordered crystalline structure, i.e., anisotropy.
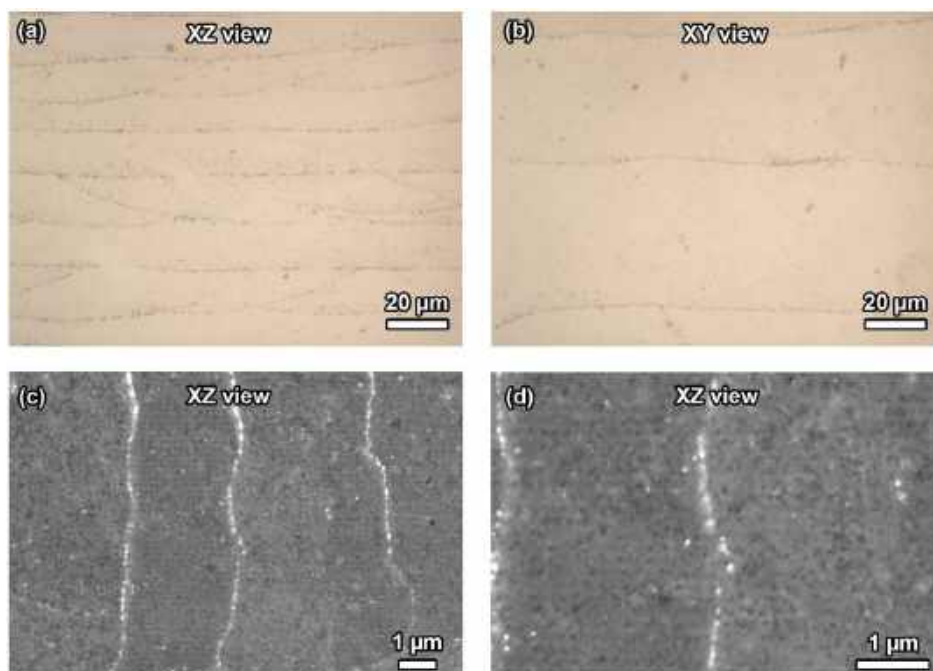

Figure 13. Microstructure of the sample C ($P_{av} = 130$ W, $v_{scan} = 1000$ mm s^{-1}). a) OM, XZ view along the building direction; b) OM, XY view perpendicular to the building direction; and c,d) BSE, XZ view along the building direction; showing the formation of Li-Ga phase during ion milling preparation (bright phase at the MP boundary).

**ADVANCED
SCIENCE NEWS**

www.advancedsciencenews.com

**ADVANCED
ENGINEERING
MATERIALS**

www.aem-journal.com

4. Discussion

In **Table 5**, the lithium concentrations for the three PBF-LB samples A, B and C, which were deduced from the measured material density and those that were identified by LIBS are summarized. In addition, the scanning speed v_{scan} is given, which is the only variable process parameter between these parameters. The applied average power and line overlap were constant ($P_{av} = 130$ W and LO = 70%).

The lithium concentrations, given in Table 5, reflect the concordant results of the two methods applied. Corresponding to the error tolerances, the lithium concentrations determined by the material density and with LIBS are comparable.

The LIBS results show a correlation between the Lithium concentration $c_{LIBS}[Li]$ and the PBF-LB parameters used: With an increasing scanning speed, the lithium concentration also rises. The higher lithium loss for lower scanning speeds can be explained by higher generated temperatures during the melting process caused by a higher deposited energy per volume, which promotes lithium evaporation. This relation could not be observed for the lithium concentrations $c_\rho[Li]$ deduced from the material density ($\rho_{material}$). The reason for this is the minor influence of the lithium content on the density. As a consequence, LIBS is more sensitive concerning the evaluation of the lithium concentration of the Al–Li alloy here.

Nevertheless, both approaches accounted for a high lithium concentration of the PBF-LB samples. The lithium content of the samples is also reflected in the mechanical properties. For the elastic modulus, as well as the Vickers hardness, the values of the additively manufactured samples were in between the two analyzed Al–Li ingots (cf. Table 4), indicating that the lithium concentration of samples A, B, and C must be in this range from 6 to 14 at%. Noble et al. reported a linear dependence between the E-modulus and the lithium content in the range of 5.5 to 14.2 at%.[5] Based on this correlation, the averaged E-modulus of sample C would correspond to a lithium concentration of 9 at%, supporting the previous findings. Furthermore, sample C showed the highest values of the mechanical properties tested, with the expectation of the highest lithium content here. Depending on the averaged hardness, the same increase in the lithium concentration could be derived from sample A to C, as already measured with LIBS. Therefore, the results of mechanical testing supplement the previous measurements and support the comparatively high lithium content of the samples fabricated with PBF-LB.

Based on the XRD analysis, the microstructure characterization and the LIBS results, it is clear that using USP-LPBF

process for Al–Li alloys of Li content higher than 9 at% successfully prevents the formation of the brittle δ-AlLi. As shown in Table 5, the Li concentration predicted from the materials density, which is based on the assumption that the constituent phase is the α-Al phase, is relative higher than those from LIBS. Thinking that the Al$_3$Li phase exhibits a density much lower than the α-Al phase, this may result from the existence of Al$_3$Li in the samples prepared by PBF-LB. The Al$_3$Li precipitated from the supersaturated α-Al phase due to intrinsic heat treatment during the PBF-LB process is supposed to improve the elastic modulus.

5. Conclusion and Outlook

This study demonstrates the potential of powder bed fusion using an USP laser system for the production of stiff, light-weight structures from highly alloyed Al–Li alloys. We identified a parameter window for a stable melting process and achieved highly dense Al–Li parts with filling factors of up to 99.7%.

The material composition of the additively manufactured samples was analyzed by ex situ laser-induced breakdown spectroscopy. The lithium concentrations achieved for the fabricated parts exceeded the value of conventional manufacturing processes. Furthermore, the dependence of the PBF-LB parameters on the lithium concentration and mechanical properties was demonstrated, showing the potential for the fabrication of Al–Li-based light-weight structures with tailored material properties.

A further increase of the lithium concentration of additively manufactured components will be the objective of further work because the mechanical performance of these parts should be enhanced accompanied by a further reduction of weight. First, the results from LIBS measurements of PBF-LB samples fabricated at lower laser powers demonstrated that the lithium concentration can exceed the values presented here. Future investigations will focus on an optimum of high density and lithium concentration. Multicomponent Al–Li alloys should also be considered here.

As already demonstrated within this work, the same laser system with comparable focusing configurations was used for the determination of the lithium content with LIBS as for the PBF-LB process. Therefore, in the next step, in situ LIBS will be implemented, where the lithium concentration can be measured directly out of the emitted spectrum generated during melting in the AM process. This approach would open up new possibilities in terms of process control and monitoring of the PBF-LB process of Al–Li alloys.

Conflict of Interest

The authors declare no conflict of interest.

Table 5. Identified values for lithium concentrations of the additive manufactured samples A, B, and C manufactured with different scanning velocities v_{scan}. $c_\rho[Li]$ is calculated from the material density (cf. Equation (4)) and $c_{LIBS}[Li]$ is the result from the LIBS analysis.

Sample	v_{scan} [mm s^{-1}]	$c_\rho[Li]$ [at%]	$c_{LIBS}[Li]$ [at%]
A	500	12.5 ± 2.2	9.1 ± 0.6
B	700	11.6 ± 2.5	10.1 ± 0.7
C	1000	11.6 ± 2.5	11.2 ± 0.4

[1] R. J. Rioja, J. Liu, *Metall. Mater. Trans. A* **2012**, *43*, 3325.

[2] A. Abd El-Aty, Y. Xu, X. Guo, S.-H. Zhang, Y. Ma, D. Chen, *J. Adv. Res.* **2018**, *10*, 49.

[3] E. N. Kablov, V. V. Antipov, J. S. Oglodkova, M. S. Oglodkov, *Metallurgist* **2021**, *65*, 172.

[4] L. Li, X. Meng, H. Zhang, P. Li, S. Huang, J. Zhou, *J. Mater. Res. Technol.* **2024**, *31*, 26.

[5] B. Noble, S. J. Harris, K. Dinsdale, *J. Mater. Sci.* **1982**, *17*, 461.

[6] E. J. Lavernia, T. S. Srivatsan, F. A. Mohamed, *J. Mater. Sci.* **1990**, *25*, 1137.

[7] N. E. Prasad, A. A. Gokhale, P. R. Rao, *Sadhana* **2003**, *28*, 209.

[8] T. Dursun, C. Soutis, *Mater. Des.* **2014**, *56*, 862.

[9] S. Jiao, X. Cheng, S. Shen, X. Wang, B. He, D. Liu, H. Wang, *J. Alloys Compd.* **2020**, *821*, 153125.

[10] D. Liu, B. Yürekli, T. Ullsperger, G. Matthäus, L. Schade, S. Nolte, M. Rettenmayr, *Mater. Des.* **2021**, *198*, 109323.

[11] O. D. Neikov, *Production of Aluminum Alloy Powders*, Elsevier **2019**, pp. 481–531, ISBN 9780081005439.

[12] R. Zhao, C. Chen, W. Wang, T. Cao, S. Shuai, S. Xu, T. Hu, H. Liao, J. Wang, Z. Ren, *Addit. Manuf.* **2022**, *51*, 102605.

[13] U. Scipioni Bertoli, G. Guss, S. Wu, M. J. Matthews, J. M. Schoenung, *Mater. Des.* **2017**, *135*, 385.

[14] M. Avateffazeli, P. Carrion, B. Shachi-Amirkhiz, H. Pirgazi, M. Mohammadi, N. Shamsaei, M. Haghshenas, *Mater. Sci. Eng.: A* **2022**, *841*, 142989.

[15] J. L. Leirmo, *Procedia CIRP* **2021**, *104*, 1747.

[16] Y. Qi, Z. Hu, H. Zhang, X. Nie, C. Zhang, H. Zhu, *Addit. Manuf.* **2021**, *47*, 102249.

[17] S. Wu, Z. Lei, B. Li, J. Liang, Y. Chen, *Addit. Manuf.* **2022**, *54*, 102762.

[18] L. Li, Y. Gou, W. Zhang, X. Meng, H. Zhang, P. Li, S. Huang, J. Zhou, *J. Alloys Compd.* **2024**, *972*, 172804.

[19] S. Shao, Z. Liang, P. Yin, X. Li, Y. Zhang, *Materials* **2024**, *17*, 657.

[20] B. Yürekli, L. Schade, T. Ullsperger, B. Seyfarth, H. Kohl, G. Matthäus, D. Liu, M. Rettenmayr, S. Nolte, *Procedia CIRP* **2020**, *94*, 69.

[21] T. Ullsperger, D. Liu, B. Yürekli, G. Matthäus, L. Schade, B. Seyfarth, H. Kohl, R. Ramm, M. Rettenmayr, S. Nolte, *Addit. Manuf.* **2021**, *46*, 102085.

[22] L. Kaden, G. Matthäus, T. Ullsperger, H. Engelhardt, M. Rettenmayr, A. Tünnermann, S. Nolte, *Appl. Phys. A* **2017**, *123*, 9.

[23] T. Ullsperger, G. Matthäus, L. Kaden, H. Engelhardt, M. Rettenmayr, S. Risse, A. Tünnermann, S. Nolte, *Appl. Phys. B* **2017**, *123*, 12.

[24] H. A. Bowman, *J. Res. Natl. Bur. Stand.* **1967**, *71*, 179.

[25] L. Schade, G. Matthäus, H. Kohl, R. Ramm, B. Yürekli, T. Ullsperger, B. Seyfarth, S. Nolte, in *Laser Powder Bed Fusion (LiM 2021)* **2021**.

[26] A. Miziolek, V. Palleschi, I. Schechter, *Laser-Induced Breakdown Spectroscopy (LIBS): Fundamentals and Applications*, Cambridge University Press **2014**.

[27] R. Noll, *Laser-Induced Breakdown Spectroscopy: Fundamentals and Applications*, Springer Berlin Heidelberg **2012**.

[28] Z. Hu, D. Zhang, W. Wang, F. Chen, Y. Xu, J. Nie, Y. Chu, L. Guo, *TrAC, Trends in Anal. Chem.* **2022**, *152*, 116618.

[29] A. Kumar, T. Jayakumar, B. Raj, K. Ray, *Acta Mater.* **2003**, *51*, 2417.

[30] G. Ben Ghorbal, A. Tricoteaux, A. Thuault, G. Louis, D. Chicot, *J. Eur. Ceram. Soc.* **2017**, *37*, 2531.

[31] V. N. Lednev, A. V. Yakovlev, T. A. Labutin, A. M. Popov, N. B. Zorov, *J. Anal. Chem.* **2007**, *62*, 1151.

[32] J. Gomba, C. D'Angelo, D. Bertuccelli, G. Bertuccelli, *Spectrochim. Acta, Part B* **2001**, *56*, 6695.

[33] P. Liu, R. Hai, D. Wu, Q. Xiao, L. Sun, H. Ding, *Plasma Sci. Technol.* **2015**, *17*, 687.

2500262 (13 of 13)

Impact of Iron Contamination on Liquid Properties and Microstructural Evolution in AlSi20

Layla Shams Tisha, Anastasiya Toenjes, and Nils Ellendt*

Additive manufacturing processes enable highly flexible and scalable shaping while maintaining rapid solidification processing conditions. This combination makes additive manufacturing particularly attractive for recycling contaminated alloys, as it allows critical brittle phases to be refined and utilized as alloying elements. However, little is known about the impact of contaminants on the fluid properties of liquid metals. Herein, thermodynamic modeling and experimental methods are combined to investigate the properties of AlSi20 and its contaminated variant, (AlSi20)95Fe5. The oscillating droplet method is used to experimentally determine surface tension and analyze solidified droplets to evaluate microstructure for different cooling rates. The findings indicate that while contaminants have a minor effect on fluid properties, they significantly influence microstructural properties.

1. Introduction

Aluminum alloys are widely used in automotive and aerospace industries, electric components, and as packaging material. Obtaining primary aluminum is a highly energy consuming process, while recycling of aluminum is more sustainable as it takes much less energy and hence produces less CO_2.[1] A significant drawback of the recycled aluminum is possible contamination with other metallic elements, iron being a common contamination among them.[2] It was found that while iron leads to embrittlement in conventional casting processes, it may lead to severe temperature-resistant strengthening if a rapid solidification process is employed to achieve finely distributed iron-rich phases.[3] Droplet solidification is commonly used as a tool to study the effect of specific cooling rates on microstructure far-off equilibrium.[4,5] Common rapid solidification processes, such as droplet

solidification or splat quenching, are often not scalable and geometrically flexible and hence could not fulfill the dream of turning scrap into high-strength materials. Spray forming[6] is a process which allows to obtain large-scale semifinished products at sufficiently high cooling rates enabling the large-scale production of rapidly solidified aluminum alloys[7] and other alloy systems. However, this process has disappeared slowly from the beginning of this millennium and was replaced by additive manufacturing approaches, such as laser powder bed fusion, which allows to produce complex parts at very high cooling rates.[8] Solidification takes place on the length scale of the melt pool with cooling rates in the range of $10^6 \, \mathrm{K \, s^{-1}}$. The interaction of the laser with the powder and the melt pool is very complex[9] and the transfer of momentum, heat, and mass in the melt pool is highly sensitive on its thermophysical properties.[10] Marangoni convection, for example, is governed by surface tension and its derivative with regard to temperature. While data on surface tension and viscosity for metallic melts are rare, even less is known if they are contaminated by specific elements. While studies exist on the thermodynamic design of alloys from the point of view of phase composition,[11] studies which incorporate the calculation of thermophysical properties of the fluid flow are rare.

In this work, we conduct a combined thermodynamic and experimental study to evaluate the effect of strong iron contamination. Hypereutectic AlSi20 is chosen as a model system, specifically contaminated with 5% iron, resulting in (AlSi20)95Fe5. To assess these alloys before producing powder for additive manufacturing experiments, thermophysical properties such as liquid density, dynamic viscosity, and surface tension, which govern the melt pool flow, are calculated. Scheil computations are conducted to investigate the effect of iron on phase formation and to evaluate the cracking susceptibility. Furthermore, surface tension is experimentally evaluated through the oscillating droplet method with a high-temperature droplet generator. The droplets are solidified during free fall in a drop tube and used to conduct a cooling rate study for main microstructural features of both alloys.

2. Results and Discussion

2.1. Thermophysical Properties

Calculations show that through the addition of iron, liquidus temperature T_L increases from 961 to 984 K. At the same time, solidus temperature T_S stays almost constant with a calculated

L. S. Tisha, A. Toenjes, N. Ellendt
Faculty of Production Engineering
University of Bremen
Badgasteiner Straße 1, 28359 Bremen, Germany
E-mail: ellendt@iwt.uni-bremen.de

L. S. Tisha, A. Toenjes, N. Ellendt
Leibniz Institute for Materials Engineering – IWT
Badgasteiner Str. 3, 28359 Bremen, Germany

The ORCID identification number(s) for the author(s) of this article can be found under https://doi.org/10.1002/adem.202401541.

decrease of only 1 K from 877 to 876 K which is related to the almost unchanged eutectic. As a result, the solidification interval increased from 84 to 108 K. Specific heat at liquidus temperature (increase from 1124 to 1129 J kg^{-1} K^{-1}) and solidus temperature (decrease from 1109 to 1108 J kg^{-1} K^{-1}) is not significantly affected by the addition of iron. Latent heat decreases by about 4% from 612 635 to 588 985 J kg^{-1}. The cracking susceptibility of AlSi20 increases from 533 to 576 K with Fe incorporation, which is in good accordance with Hren et al.[12]

Liquid density, dynamic viscosity, and surface tension have major impact on the flow field of liquid melt in a melt pool.

The calculated liquid density as a function of melt superheat with regard to liquidus is shown in **Figure 1**a. The addition of iron increases density at liquidus σ_L from 2491 to 2633 kg m^{-3}. Density decreases linearly with a similar slope $\frac{\partial \sigma}{\partial T}$ of 0.343 and 0.363 kg m^{-3} K^{-1} for AlSi20 and (AlSi20)95Fe5, respectively. Viscosity is also increased through the addition of iron (Figure 1b). The addition of iron leads to a minor increase of the prefactor η_0 from 0.2328 to 0.2350 mPa s. Also, the activation energy E_A for viscous flow is increasing slightly from 14 761 to 15 881 J mol^{-1}. Resultingly, there is a small shift of dynamic viscosity up by ≈0.1 mPa s as iron is added. Determined properties are summarized in **Table 1**.
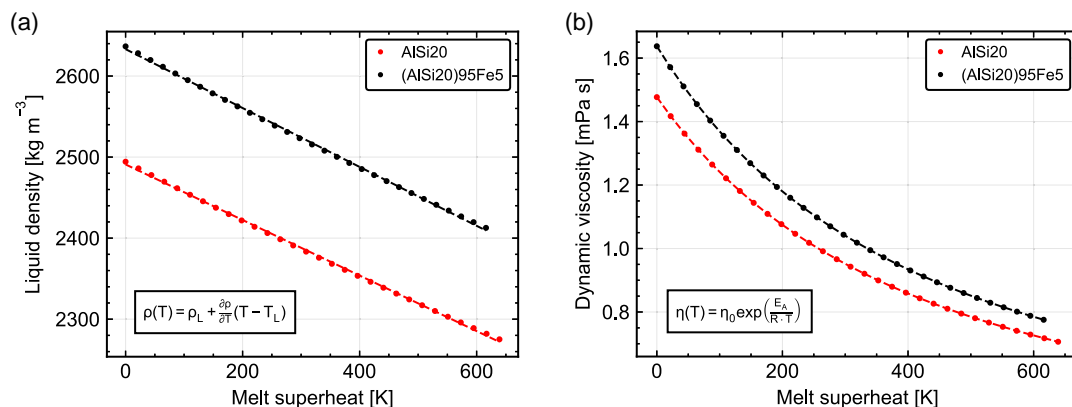

Figure 1. Calculated a) liquid density and b) dynamic viscosity; melt superheat is calculated with respect to liquidus temperature. Points indicate calculated data points; dotted lines show determined model equations.

Table 1. Determined properties of AlSi20 and (AlSi20)95Fe5.

	AlSi20	(AlSi20)95Fe5
Liquidus T_L [K]	$T_L = 961$ K	$T_L = 984$ K
Solidus T_S [K]	$T_S = 877$ K	$T_S = 876$ K
Solidification interval [K]	$T_L - T_S = 84$ K	$T_L - T_S = 108$ K
Specific heat $c_{p,L}$ at liquidus [J kg^{-1} K^{-1}]	$c_{p,L} = 1124$ J kg^{-1} K^{-1}	$c_{p,L} = 1129$ J kg^{-1} K^{-1}
Specific heat $c_{p,S}$ at solidus [J kg^{-1} K^{-1}]	$c_{p,S} = 1109$ J kg^{-1} K^{-1}	$c_{p,S} = 1108$ J kg^{-1} K^{-1}
Latent heat L [J kg^{-1}]	$L = 612\ 635$ J kg^{-1}	$L = 588\ 985$ J kg^{-1}
Liquid density [kg m^{-3}]	$\rho_L = 2491$ kg m^{-3}	$\rho_L = 2663$ kg m^{-3}
$\rho(T) = \rho_L - \frac{\partial \rho}{\partial T}(T - T_L)$	$\frac{\partial \rho}{\partial T} = 0.3427$ kg m^{-3} K^{-1}	$\frac{\partial \rho}{\partial T} = 0.3633$ kg m^{-3} K^{-1}
Surface tension [N m^{-1}]	$\sigma_L = 0.883$ N m^{-1}	$\sigma_L = 0.881$ N m^{-1}
$\sigma(T) = \sigma_L - \frac{\partial \sigma}{\partial T}(T - T_L)$	$\frac{\partial \sigma}{\partial T} = 1.496 \times 10^{-4}$ N m^{-1} K^{-1}	$\frac{\partial \sigma}{\partial T} = 1.456 \times 10^{-4}$ N m^{-1} K^{-1}
Surface tension [N m^{-1}][a]	$\sigma_L = 0.819$ N m^{-1}	$\sigma_L = 0.819$ N m^{-1}
$\sigma(T) = \sigma_L + \frac{\partial \sigma}{\partial T}(T - T_L)$	$\frac{\partial \sigma}{\partial T} = 1.431 \times 10^{-4}$ N m^{-1} K^{-1}	$\frac{\partial \sigma}{\partial T} = 2.071 \times 10^{-4}$ N m^{-1} K^{-1}
Dynamic viscosity [mPa s]	$\eta_0 = 0.2382$ μPa s	$\eta_0 = 0.2350$ μPa s
$\eta(T) = \eta_0 \exp\left(\frac{E_A}{R \times T}\right)$	$E_A = 14761.683$ J mol^{-1}	$E_A = 15881.336$ J mol^{-1}
Cracking susceptibility [K]	$\Phi = 533$ K	$\Phi = 576$ K
$\Phi = \left.\frac{dT}{df_s^{\frac{1}{2}}}\right|_{max}$		

[a]Measured properties are indicated with *; all other values are calculated.

Surface tension was calculated with the Butler equation and measured through the droplet oscillation method.

Figure 2 shows an exemplary droplet oscillation as acquired with the high-speed camera for a droplet of AlSi20 with a diameter of 1.4 mm and a temperature of 1300 °C. The droplet detaches with an initial deformation in the first frame and then oscillates during free fall in the argon atmosphere. After image analysis, an oscillation, as shown in **Figure 3**a, is obtained. Fitting of this data with the equation of the dampened harmonic oscillator allows to determine the oscillation frequency and hence the surface tension through the Rayleigh equation.

Figure 3b compares measured and calculated surface tension for both alloys and compares with a reference for the surface tension of AlSi20. It can be seen that the calculation results for both alloys are very similar. Surface tension values at liquidus σ_L of 0.883 and 0.881 N m^{-1} as well as temperature coefficients $\frac{\partial \sigma}{\partial T}$ of 1.496×10^{-4} and 1.456×10^{-4} N m^{-1} K^{-1} were obtained for AlSi20 and (AlSi20)95Fe5, respectively. Measured values of surface tension are in a similar value range for both alloys and show good accordance with the experimental correlation of Kobatake et al.[13] Also, good agreement to calculated values is achieved.

2.2. Microstructure Development

The droplets used for measurement of surface tension were solidified in free fall and quenched in water. Their cooling rate was determined with a validated model. Apparent specific heat from thermodynamic calculation was used to model solidification through the heat capacity method. **Figure 4**a shows the thermal history of two droplets of AlSi20 with diameters 270 and 720 μm. The cooling rate during solidification is determined from each thermal history. Figure 4b summarizes the average cooling rates during solidification of both alloys as a function of droplet diameter. No major difference was found in between the two alloys.

We obtained $\frac{dT}{dt} = 3.989 \times 10^{-5} d^{1.889}$ and $\frac{dT}{dt} = 5.516 \times 10^{-5} d^{1.887}$ for AlSi20 and (AlSi20)95Fe5, respectively.

Figure 5 shows the microstructure of droplets of AlSi20 alloy, having different diameters. The microstructure shows significant presence of primary Si phases in the droplets. It is observed that the primary silicon phases are formed within the eutectic needle structure. As the droplet diameter increases, also the primary Si dispersoids become larger.

The elemental composition of a solidified AlSi20 droplet was analyzed through energy-dispersive spectrometer (EDS). **Figure 6** displays the elemental mapping of the sample for Al and Si. Figure 6a shows a significant presence of Si, proving the dispersoids to be primary Si. The presence of Si is also detected in the needle-like phases (Figure 6d), suggesting that the eutectic needle-like structures incorporate Si element. Other than Si, Al distribution is found as matrix phase (Figure 6c).

This is in agreement with a Scheil calculation (**Figure 7**a), where we can see that the eutectic needle and the primary Si start forming simultaneously. As the droplet size decreases, cooling rate increases leading to a reduction of the size of primary Si (Figure 7b). This happens due to the shorter time interval for the growth of primary Si phase and higher undercooling, resulting in smaller and more frequent dispersoids.

For (AlSi20)95Fe5, a seaweed morphology is found only for the largest particle size. Smaller droplets feature a typical dendritic structure with an iron-rich eutectic (**Figure 8**). Dendritic spacing becomes smaller as droplet size decreases and cooling rate increases, resultingly.
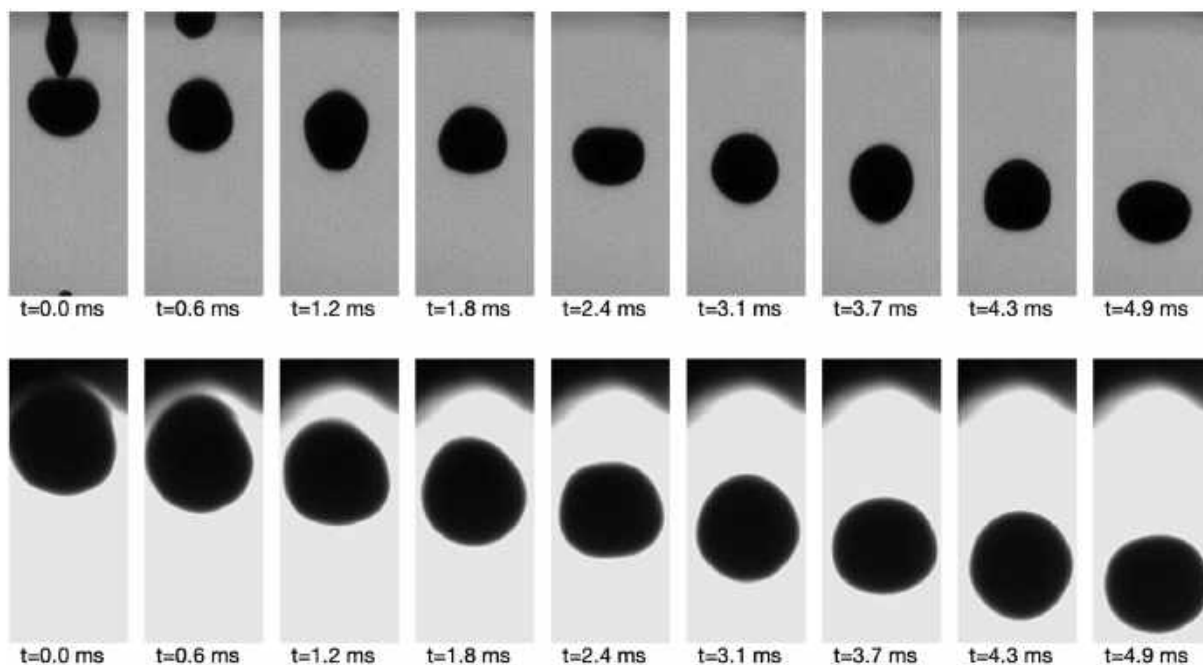

Figure 2. Exemplary image sequence of oscillating droplet and after detachment and subsequent oscillation (above: AlSi20, droplet diameter: 1.4 mm, temperature: 1300 °C; below: (AlSi20)95Fe5, droplet diameter: 1.6 mm, temperature: 1040 °C).
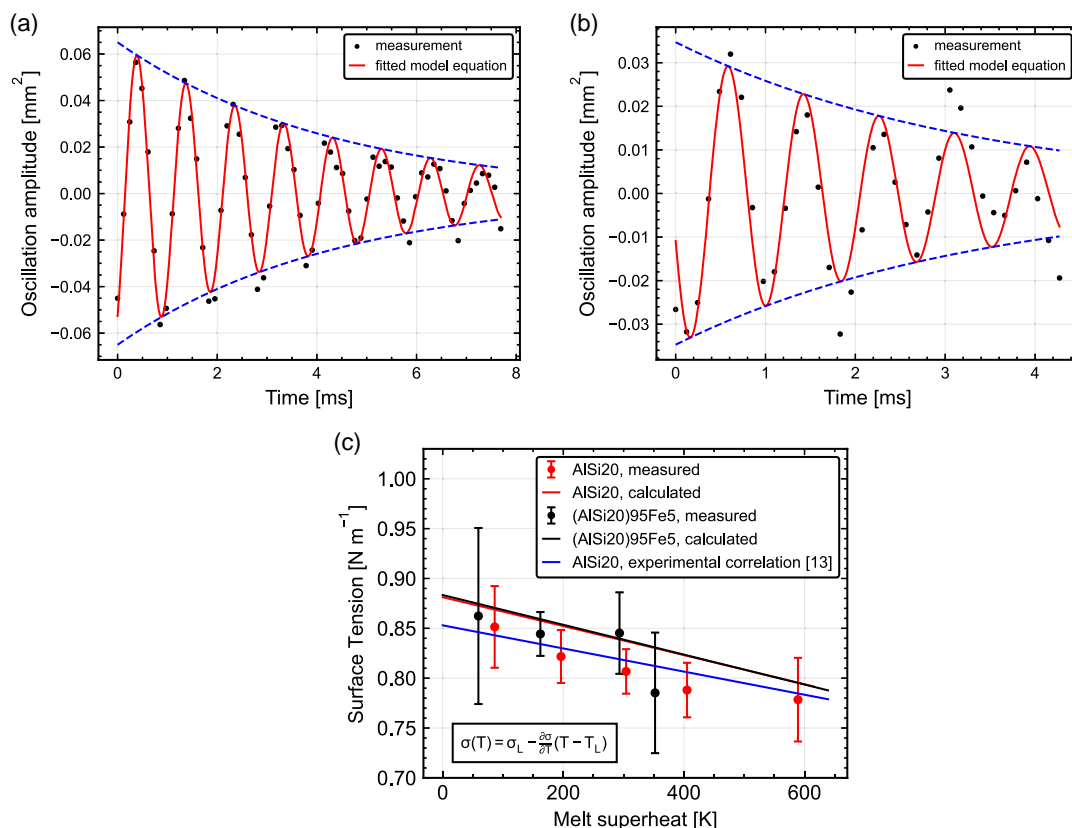
**ADVANCED
SCIENCE NEWS**

www.advancedsciencenews.com

**ADVANCED
ENGINEERING
MATERIALS**

www.aem-journal.com

Figure 3. Exemplary measured droplet oscillation and fitted model equation a) AlSi20, diameter: 803 µm, temperature: 1300 °C resulting in an oscillation frequency of 1019 Hz and a surface tension of 0.814 N m^{-1}; b) (AlSi20)95Fe5, diameter: 803 µm, temperature: 1040 °C, resulting in an oscillation frequency of 1167 Hz and a surface tension of 0.714 N m^{-1}; and c) comparison of measured surface tension for both alloy as function of temperature. Our calculated relationships and an experimental relationship from Kobatake et al.[13] show good agreement.
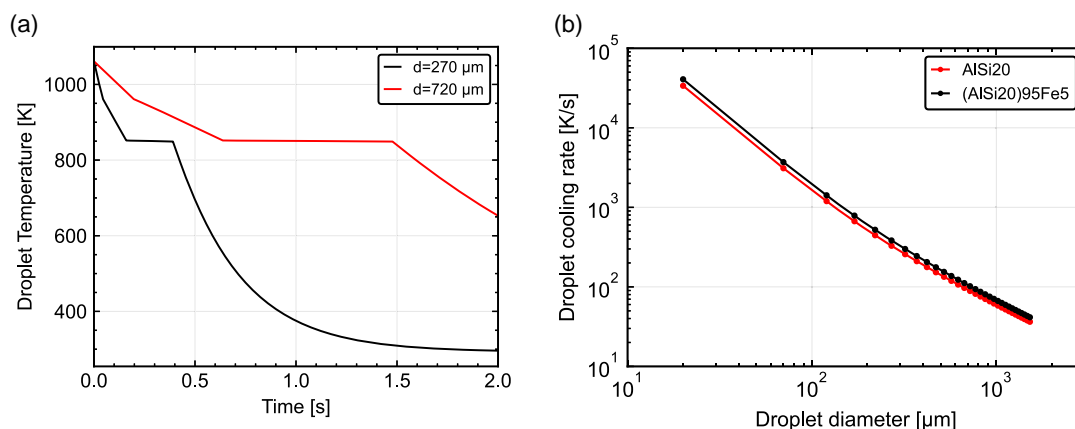

Figure 4. a) Calculated thermal history of two droplets with different diameters (alloy: AlSi20). b) Resulting correlation between droplet cooling rate during solidification and droplet diameter.

Figure 9 represents the elemental mapping of a solidified (AlSi20)95Fe5 droplet obtained through EDS analysis for Al, Si and Fe. A prominent amount of Al is determined in the dendritic structure (Figure 9b). An Si-rich eutectic matrix is detected as well (Figure 9c) with a homogeneous distribution of Fe throughout the entire particle (Figure 9d). No trace of primary Si phase is found in the EDS analysis. This result aligns well with the existing work.[14,15]

The absence of primary silicon is in agreement with a Scheil calculation for (AlSi20)95Fe5 (**Figure 10**a). Instead of primary

**ADVANCED
SCIENCE NEWS**

www.advancedsciencenews.com

**ADVANCED
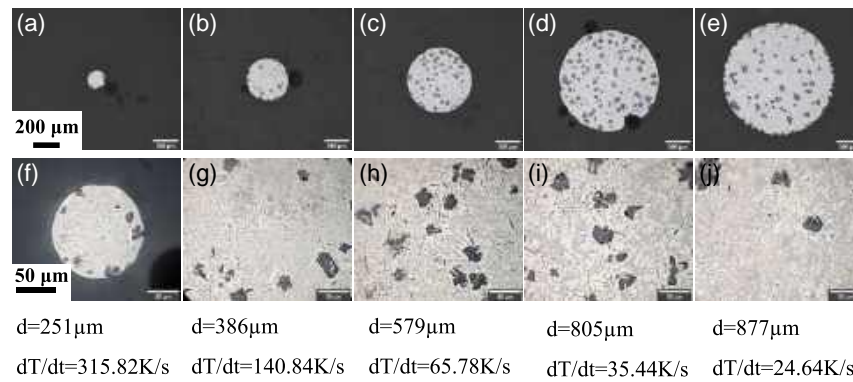ENGINEERING
MATERIALS**

www.aem-journal.com

Figure 5. Microstructure of AlSi20 droplets solidified during free falling with a diameter range of 251–877 μm and resultingly different cooling rate. a–e) The microscopic image of full size solidified droplet. f–j) Detailed microstructural features.
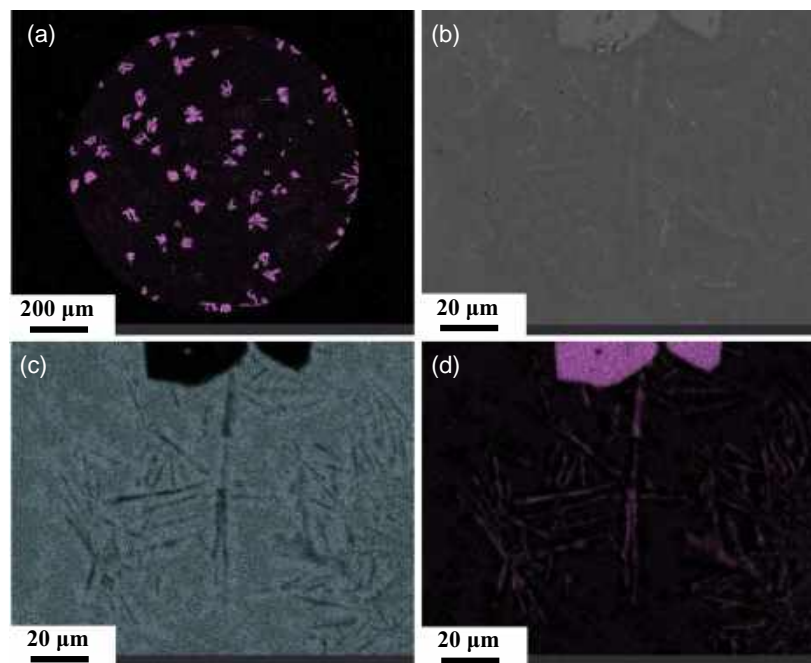

Figure 6. Elemental mapping from energy-dispersive X-ray spectroscopy obtained from of AlSi20 droplet, diameter = 877 μm, showing the a) entire droplet, b) selected region of interest, c) Al composition, and d) Si composition.
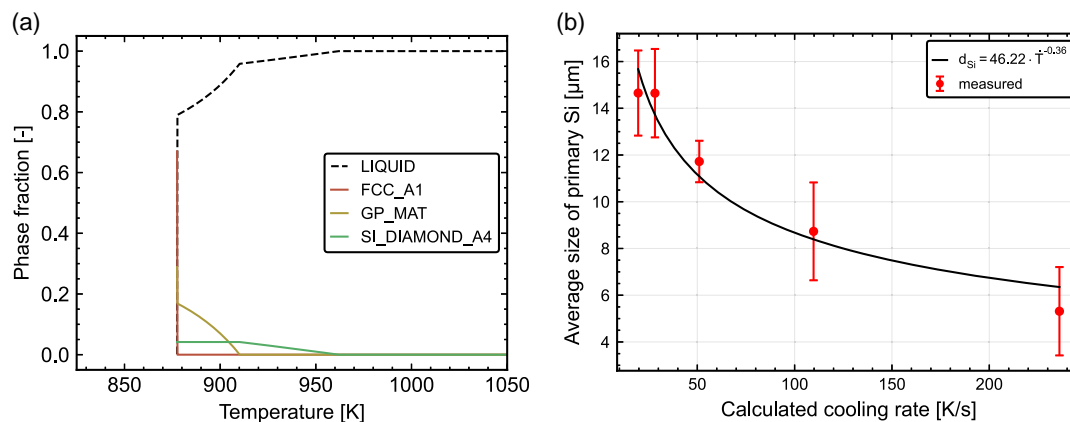

Figure 7. a) Scheil calculation of solidification of AlSi20 showing the composition of phases during solidification. b) The determined relationship between size of primary silicon and calculated cooling rate for each droplet size.
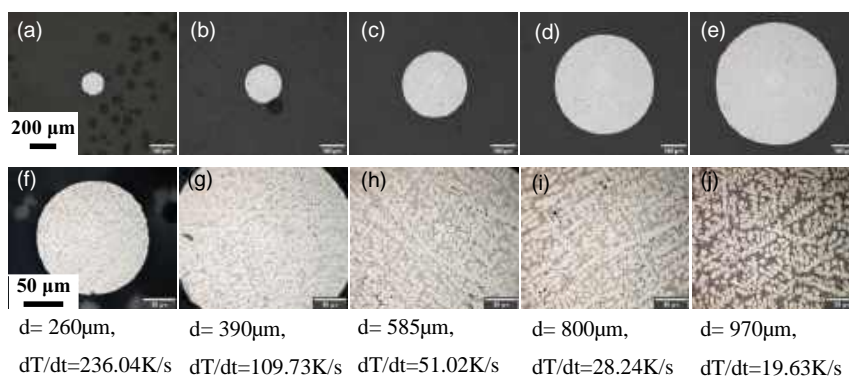
Figure 8. Microstructure (AlSi20)95Fe5 droplets solidified during free-falling with a diameter range of 260–970 μm and resultingly different cooling rate. a–e) The microscopic image of full size solidified droplet. f–j) Detailed microstructural features.
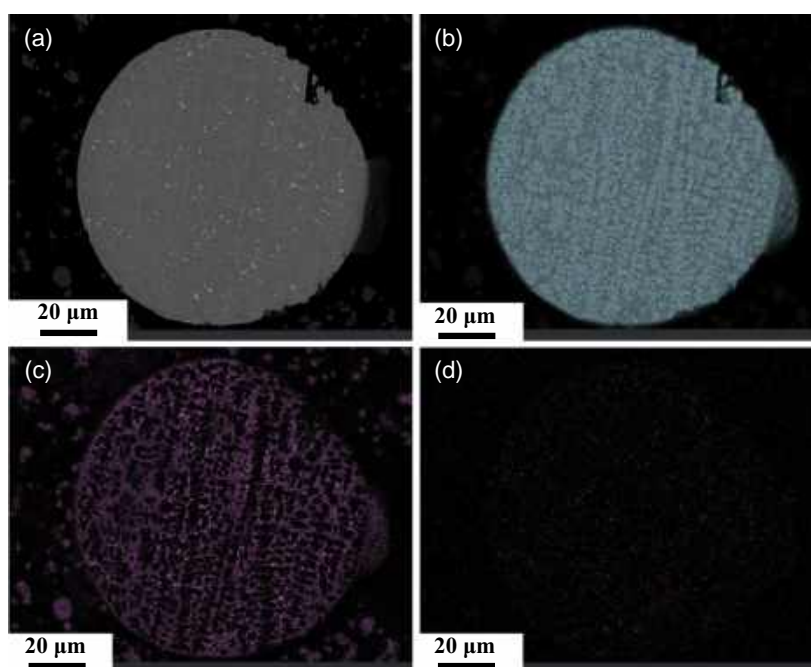

Figure 9. Elemental mapping from energy-dispersive X-ray spectroscopy obtained from of (AlSi20)95Fe5 droplet, diameter = 260 μm, showing the a) entire droplet, b) Al composition, c) Si composition, and d) Fe composition.
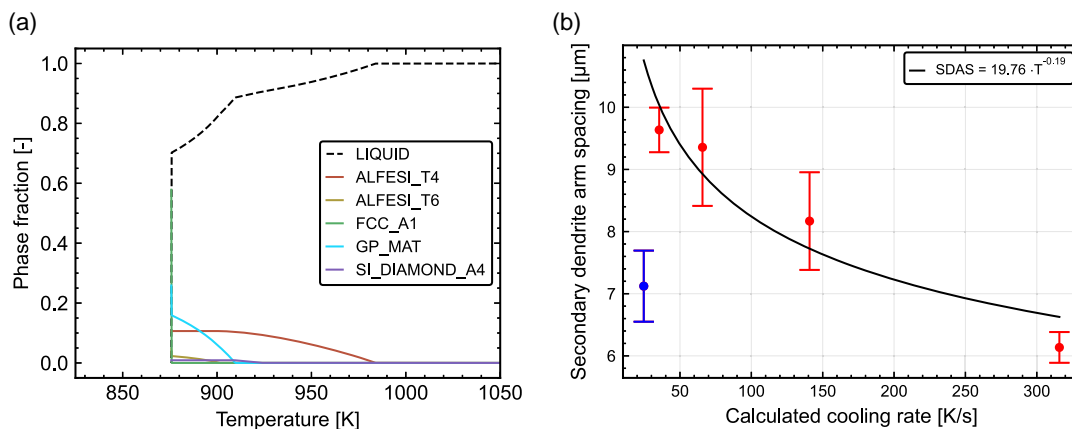

Figure 10. a) Scheil calculation of solidification of (AlSi20)95Fe. b) The determined relationship between size of primary silicon and calculated cooling rate for each droplet size. The blue data point features a different morphology and was not taken into account for the correlation.

silicon, two iron-rich Al–Fe–Si phases are formed leaving only a negligible amount of Si available for primary precipitation. For a deeper insight, the secondary dendrite arm spacing was measured (Figure 10b). Due to a morphology change in between the particles with diameters of 800 and 970 μm, only the particles with diameter of ≤800 μm were taken into account for the determination of the correlation.

From the Scheil calculations, the cracking susceptibility was determined to be 533 K for AlSi20 and 576 K for (AlSi20) 95Fe5, hence an increase of around 8%. This is related not only to other phases being formed, but also to the increase of the solidification interval from 84 to 108 K.

3. Conclusion

In this work, we conducted a comprehensive thermodynamic study of thermodynamic and fluid properties, supplemented by a droplet-based experimental investigation of surface tension and a cooling rate-dependent microstructural analysis. We demonstrated that, prior to performing additive manufacturing experiments (including the production or blending of powders), major differences and similarities between different alloy compositions can be identified.

As expected, liquid density increases with the addition of iron due to its much higher density compared to aluminum and silicon. However, surface tension is affected only to a minor extent, which was confirmed through an experimental analysis using the oscillating droplet method. Our experimental findings for pure AlSi20 are in quantitative agreement with experimental data from other authors. Dynamic viscosity remains almost unaffected. From this, we conclude that, from the perspective of fluid dynamics, the flow in the melt pool will not be significantly affected by contamination with 5 wt% iron.

Scheil calculations indicate that the addition of iron in the given quantity leads to the formation of iron-rich AlSiFe phases, which suppresses the precipitation of primary silicon. This is a major difference between the two alloys and also leads to an increase in cracking susceptibility by 8%. The results of the Scheil computation are supported by the quantitative microstructural analyses of droplets solidified in argon during free fall. We derived correlations between cooling rate and the size of primary silicon in AlSi20 and secondary dendrite arm spacing in (AlSi20) 95Fe5. Even though these cooling rates are much smaller than those achieved in powder bed fusion, average primary silicon sizes of 5 μm and secondary dendrite arm spacings of 6 μm for cooling rates of $\approx300\,\mathrm{K\,s^{-1}}$ already indicate that sufficiently fine microstructures will be obtained at cooling rates in the order of $10^6\,\mathrm{K\,s^{-1}}$.

4. Experimental Section

Droplet Experiments: Feedstock material of the two alloys AlSi20 and AlSi19Fe5 was prepared from high purity elements (each 99.99%) in an arc melter (Bühler MAM-1) in a high-purity, Ti-gettered atmosphere. Samples were turned 3 times to provide solution of all elements. The material was then melted in a high-temperature droplet generator[16] in an Argon atmosphere with an oxygen content <20 ppm. The material was molten and then heated to the lowest temperature before droplets were generated. A Graphite crucible with a nozzle diameter of 560 μm

was used for both alloys. In order to prevent the high wetting problem of Al–Si alloy, a thin layer of boron nitride was sprayed at the bottom of the crucible. The droplets were produced in the temperature range of 750–1200 °C. Droplet detachment and oscillation was recorded with a high-speed camera (Photron UX50) before the melt was heated to the next temperature. The droplets solidified during a falling distance of 6.5 m in argon atmosphere and were collected for analysis. Recorded droplet oscillations were analyzed through fitting of a harmonic oscillator equation:

$$A(t) = A_0 \cos(\omega \cdot t) \cdot \exp(-\tau \cdot t) \tag{1}$$

Surface tension can be calculated from the oscillation frequency ω through the Rayleigh equation:[17]

$$\omega^2 = \frac{32\pi}{3}\frac{\sigma}{M} \tag{2}$$

Details about this experimental approach can be found in ref. [18].

Microstructure Analyses: Particles generated at the droplet generator are categorized according to their diameter size. Five size classes from each alloy (250–1000 μm) with each an interval width of 10 μm were taken and they were embedded and conventionally polished for the microstructure analysis. A Zeiss Axio Imager light microscope was used for the analysis and ImageJ[19] was used to determine the distribution of primary silicon size and secondary dendrite arm spacing. In order to maintain a good accuracy and precisions, we measured for each particle size and at least five dendrites. The individual measurements were then averaged to have an averaged value for each data point.

Calculations: Thermodynamic Calculations: For the calculation of surface tension, the Butler equations[20]

$$\sigma = \sigma_i + \frac{RT}{A_i}\ln\left(\frac{x_i^S}{x_i^B}\right) + \frac{G_{s,i}^{xs} - G_{b,i}^{xs}}{A_i} \tag{3}$$

are solved for the binary and ternary case. Viscosity was obtained through the Kaptay equation:[21,22]

$$\eta = \frac{h\,N_A}{\left(\sum_i x_i\nu_i\right) + \nu^e}\exp\left(\frac{\left(\sum_i x_i G_i^*\right) - (0.155 \pm 0.015)H_M}{RT}\right) \tag{4}$$

To calculate the liquid density, the model by Liu et al.[23]

$$V = \overline{V}\exp(\Lambda\Delta H^{xs})\,\Lambda = \sum X_i\Lambda_i = \sum X_i\left(\frac{\beta_i}{c_{p,i}}\right) \tag{5}$$

was used to calculate molar volume of the liquid, which was then converted to density. Details about these models can be found in their corresponding publications. The equations were implemented within the Open Source framework of PyCalphad.[24] MatCalc's free thermodynamic database for aluminum alloys (version 2.036) was used to provide thermodynamic quantities. Further properties needed were taken from refs. [25,26]. Scheil calculations were carried out with the Scheil package[24] for PyCalphad. Cracking susceptibility was determined from the maximum slope of solid fraction f_s with the square root of temperature[27,28] as

$$\Phi = \left.\frac{dT}{df_s^{\frac{1}{2}}}\right|_{max} \tag{6}$$

Calculations: Cooling Rate Calculations: A validated cooling rate model[29] was used to calculate the cooling rate of different droplet sizes. The trajectory equation and temperature equation

$$\frac{d\nu}{dt} = g - \frac{3}{4d_p}c_D\cdot\frac{\rho_F}{\rho_P}\cdot\nu^2 \tag{7}$$

$$d\rho_p c_p \frac{dT_p}{dt} = -6\left[h(T_p - T_\infty) + \sigma\varepsilon(T_p^4 - T_\infty^4)\right] \tag{8}$$

were solved utilizing a temperature-dependent correlation for the drag coefficient.[30] Temperature-dependent apparent specific heat was calculated with PyCalphad for both alloys and used in the code to model the solidification interval. For each droplet size, solidification time was calculated and the ratio of solidification range and solidification time was calculated as an average cooling rate during solidification.

Acknowledgements

Conflict of Interest

The authors declare no conflict of interest.

Author Contributions

Layla Shams Tisha: Data curation (lead); Investigation (lead); Writing—original draft (lead); Writing—review and editing (lead). **Anastasiya Toenjes**: Conceptualization (supporting); Funding acquisition (equal); Supervision (supporting); Validation (lead); Writing—review and editing (equal). **Nils Ellendt**: Conceptualization (lead); Funding acquisition (equal); Supervision (lead); Writing—review and editing (equal).

Data Availability Statement

The data that support the findings of this study are available from the corresponding author upon reasonable request.

Keywords

[1] J. C. González Palencia, T. Furubayashi, T. Nakata, *Energy Policy* **2013**, *52*, 328.

[2] J. A. Taylor, in *35th Australian Foundry Institute National Conf.*, Australian Foundry Institute (AFI) Adelaide, October 31st–November 3rd, South Australia **2004**.

[3] H. Henein, V. Buchoud, R.-R. Schmidt, C. Watt, D. Malakov, C.-A. Gandin, G. Lesoult, V. Uhlenwinkel, *Can. Metall. Q.* **2013**, *49*, 275.

[4] O. E. Jegede, R. F. Cochrane, A. M. Mullis, *J. Mater. Sci.* **2018**, *53*, 11749.

[5] N. Ciftci, N. Ellendt, G. Coulthard, E. Soares Barreto, L. Mädler, V. Uhlenwinkel, *Metall. Mater. Trans. B* **2019**, *50*, 666.

[6] P. Krug, in *Metal Sprays and Spray Deposition* (Eds: H. Henein, V. Uhlenwinkel, U. Fritsching), Springer International Publishing, Cham **2017**, pp. 379–406.

[7] B. V. R. Reddy, S. R. Maity, K. M. Pandey, *Rev. Adv. Mater. Sci.* **2019**, *58*, 147.

[8] C. L. Druzgalski, A. Ashby, G. Guss, W. E. King, T. T. Roehling, M. J. Matthews, *Addit. Manuf.* **2020**, *34*, 101169.

[9] C. Bierwisch, B. Dietemann, T. Najuch, *Granular Matter* **2024**, *26*, 71.

[10] A. Chouhan, M. Hesselmann, A. Toenjes, L. Mädler, N. Ellendt, *Addit. Manuf.* **2022**, *59*, 103179.

[11] Z. Sun, Y. Ma, D. Ponge, S. Zaefferer, E. A. Jägle, B. Gault, A. D. Rollett, D. Raabe, *Nat. Commun.* **2022**, *13*, 4361.

[12] I. Hren, J. Svobodova, Michna, *Arch. Foundry Eng.* **2018**, *18*, 120.

[13] H. Kobatake, J. Brillo, J. Schmitz, P.-Y. Pichon, *J. Mater. Sci.* **2015**, *50*, 3351.

[14] P. Mikolajczak, L. Ratke, *Metall. Mater. Trans. A* **2015**, *46*, 1312.

[15] Q. Li, Y. Zhu, B. Li, W. Ding, Y. Lan, T. Xia, Q. Du, *Mater. Res. Express* **2019**, *6*, 016506.

[16] S. Imani Moqadam, L. Mädler, N. Ellendt, *Micromachines* **2019**, *10*, 477.

[17] L. Rayleigh, *Proc. R. Soc. Lond.* **1879**, *29*, 71.

[18] K. Fahimi, L. Mädler, N. Ellendt, *Exp. Fluids* **2023**, *64*, 133.

[19] J. Schindelin, I. Arganda-Carreras, E. Frise, V. Kaynig, M. Longair, T. Pietzsch, S. Preibisch, C. Rueden, S. Saalfeld, B. Schmid, J.-Y. Tinevez, D. J. White, V. Hartenstein, K. Eliceiri, P. Tomancak, A. Cardona, *Nat. Methods* **2012**, *9*, 676.

[20] J. A. V. Butler, *Proc. R. Soc. London, Ser. A* **1932**, *135*, 348.

[21] G. Kaptay, in *Proc. microCAD Conf., Section Metallurgy*, University of Miskolc, Hungary, March 6t-h7th, **2003**.

[22] F. Zhang, S. Wen, Y. Liu, Y. Du, G. Kaptay, *J. Mol. Liq.* **2019**, *291*, 111345.

[23] Y. Liu, Y. H. Liu, X. P. Su, *Calphad* **2020**, *68*, 101690.

[24] B. Bocklund, L. D. Bobbio, R. A. Otis, A. M. Beese, Z.-K. Liu, pycalphad-scheil: 0.1.6, Zenodo **2020**.

[25] H. Fukuyama, H. Higashi, M. Adachi, M. Ohtsuka, *High Temp. Mater. Processes* **2023**, *42*, 20220286.

[26] T. Iida, R. I. L. Guthrie, in *The Thermophysical Properties of Metallic Liquids: Volume 1 — Fundamentals*, Oxford University Press, Oxford, United Kingdom, **2015**.

[27] H. Hyer, L. Zhou, A. Mehta, Y. Sohn, *J. Phase Equilib. Diffus.* **2021**, *42*, 5.

[28] S. Kou, *Acta Mater.* **2015**, *88*, 366.

[29] S. Imani Moqadam, L. Mädler, N. Ellendt, *Materials* **2019**, *12*, 3769.

[30] N. Ellendt, A. M. Lumanglas, S. I. Moqadam, L. Mädler, *Int. J. Therm. Sci.* **2018**, *133*, 98.